TU Delft

Delft University of Technology

Document Version
Final published version

Licence
Dutch Copyright Act (Article 25fa)

Citation (APA)
Mahmoudiniya, M., Luyten, B., Ghavanini, N., Verleysen, P., Hermans, M., & Kestens, L. A. I. (2026). Microstructure, texture and mechanical performance of a nickel–aluminium bronze / martensitic stainless steel bimetal produced by direct energy deposition. *Materials Science and Engineering: A*, *961*, Article 150140. https://doi.org/10.1016/j.msea.2026.150140

Important note
To cite this publication, please use the final published version (if applicable).
Please check the document version above.

Copyright
In case the licence states “Dutch Copyright Act (Article 25fa)”, this publication was made available Green Open Access via the TU Delft Institutional Repository pursuant to Dutch Copyright Act (Article 25fa, the Taverne amendment). This provision does not affect copyright ownership.
Unless copyright is transferred by contract or statute, it remains with the copyright holder.

Sharing and reuse
Other than for strictly personal use, it is not permitted to download, forward or distribute the text or part of it, without the consent of the author(s) and/or copyright holder(s), unless the work is under an open content license such as Creative Commons.

Takedown policy
Please contact us and provide details if you believe this document breaches copyrights.
We will remove access to the work immediately and investigate your claim.

This work is downloaded from Delft University of Technology.

Materials Science & Engineering A 961 (2026) 150140

Contents lists available at ScienceDirect

Materials Science & Engineering A

journal homepage: www.elsevier.com/locate/msea

Microstructure, texture and mechanical performance of a nickel–aluminium bronze / martensitic stainless steel bimetal produced by direct energy deposition

Mahdi Mahmoudiniya [a,*], Briek Luyten [a], Navid Ghavanini [a], Patricia Verleysen [a], Marcel Hermans [b], Leo A.I. Kestens [a,b]

[a] Ghent University, Metals Science and Technology Group, Technologiepark 903 B-9052 Zwijnaarde, Ghent, Belgium
[b] Delft University of Technology, Department of Materials Science and Engineering, Mekelweg, 22628 CD, Delft, the Netherlands

ARTICLE INFO

Keywords:
Bimetallic structure
Wire arc additive manufacturing
Nickel aluminium bronze
Martensitic stainless steel
Microstructure and texture
Interfacial properties

ABSTRACT

This study investigates the microstructural evolution, crystallographic texture, and mechanical properties of a nickel-aluminium bronze (NAB)/410 NiMo martensitic stainless steel bimetallic structure fabricated via wire arc additive manufacturing (WAAM). The work provides a detailed assessment of the interfacial characteristics, phase transformations, and texture development across both alloys, as well as their impact on mechanical behaviour. Microstructural characterisation using optical microscopy, SEM, EBSD, and TEM revealed that the stainless steel region predominantly consists of martensite with minor fractions of δ-ferrite, α-ferrite, and retained austenite. A distinct Fe-rich interfacial layer was identified, from which columnar dendrites grow epitaxially into the NAB side. The NAB region exhibits α-phase grains with various *k*-phase precipitates whose distribution and morphology evolve with build height due to thermal cycling and dilution effects. Evidence of liquid metal embrittlement (LME) was observed at the interface. Texture analysis indicated a weak crystallographic texture in the stainless steel due to solid-state transformations, whereas the NAB exhibited a more textured structure, especially <101>//BD. Despite the presence of LME cracks at the interface, tensile testing consistently resulted in fracture within the NAB region, away from the interface, demonstrating effective load transfer across the interface under uniaxial tensile loading parallel to the building direction. The bimetallic structure achieved an ultimate tensile strength of 587 MPa and total elongation of ~12%.

1. Introduction

Wire arc additive manufacturing (WAAM) is regarded as one of the primary additive manufacturing techniques for fabricating large metallic components. Specific characteristics, such as a high deposition rate (up to 15 kg/h), efficient material usage, and cost-effectiveness, render WAAM a promising method for producing not only mono-metallic large parts but also large multi-metallic components [1]. The integration of two distinct materials into a single structure is considered a powerful method for achieving enhanced and localised performance. By strategically placing materials with tailored properties, engineers can create components that more efficiently meet complex functional requirements. This design versatility opens up new possibilities across various industries, thereby driving increasing interest in the development and manufacturing of multi-material systems [2] [3].

The bimetallic combination of bronze and stainless steel (SS) is of great importance in marine applications, particularly for propeller production. Bronze alloys offer excellent corrosion and cavitation resistance in seawater and possess good wear properties [4], while stainless steels can provide high mechanical strength and toughness [5]. By combining these two materials, it is possible to produce components that withstand harsh marine environments whilst maintaining structural integrity and durability. This synergy makes the bronze–stainless steel combination particularly advantageous for high-performance and long-lasting propeller systems [6].

Despite the promising benefits of combining bronze (a copper-based alloy) with stainless steel, manufacturing such bimetallic components presents significant challenges due to the fundamental dissimilarities in their physical, chemical, and thermo-mechanical properties. Issues such as solidification and liquation cracking often occur at the interface due

* Corresponding author.
E-mail address: mahdi.mahmoudiniya@Ugent.be (M. Mahmoudiniya).

https://doi.org/10.1016/j.msea.2026.150140
Received 21 October 2025; Received in revised form 18 March 2026; Accepted 22 March 2026
Available online 26 March 2026
0921-5093/© 2026 Elsevier B.V. All rights are reserved, including those for text and data mining, AI training, and similar technologies.

to a mismatch in thermal expansion and conductivity, resulting in high residual stresses [7] [8]. Furthermore, the limited solubility between Cu and Fe results in interfacial segregation and weak bonding, diminishing mechanical performance [9]. Given these challenges, recent research has increasingly concentrated on exploring the additive manufacturing of copper alloy–stainless steel hybrid components. Most of this research has utilised a laser as the heating source for the AM process. In this regard, Liu et al. [7] used selective laser melting (SLM) to produce 316L stainless steel/CuCrZr alloy hybrid material. Although the tensile properties were reported to be satisfactory, they reported the formation of some solidification cracks at the interface. Chen et al. [9] also used SLM to build a 316L/CuSn10 bimetallic structure. They also observed dendritic cracks at the boundary between the bimetallic fusion zone and the steel. Although they managed to minimise solidification cracking by optimising processing parameters, it was not possible to eliminate it. Despite the benefits of laser-based AM techniques, their usage in the production of this specific bimetallic structure has had challenges: (a) the copper exhibits high reflectivity to lasers, which are widely used in industrial applications, and it absorbs less than 5% of the incident laser energy, which makes the effective melting and deposition of copper highly challenging [10](b) High heating and cooling rates are characteristic of laser processing due to the focused nature of the laser. This intensifies the formation of defects and incompatibilities between two different materials.

Using an electric arc as the heat source may alleviate limitations of the high reflectivity of the copper and the high heating and cooling rates of laser-based AM techniques for the production of bronze/stainless steel hybrid components [11] [12]. However, there is not much literature reported on this subject. Dharmendra et al. [13] printed a nickel aluminium bronze (NAB) on a block of 316 austenitic stainless steel using gas metal arc welding (GMAW). They observed good metallurgical bonding at the interface, and solidification cracks were not present. However, they noted liquid metal embrittlement (LME) phenomena in the heat-affected zone (HAZ) of 316 stainless steel. To the authors' knowledge, there is no reported study on using WAAM for the production of nickel-aluminium bronze-martensitic stainless steel bimetallic components. The present study aims to investigate the production of a bimetallic structure composed of nickel aluminium bronze and 410 NiMo martensitic stainless steel using WAAM with the focus is on understanding microstructural development and interface properties.

2. Materials and methods

The bronze/steel hybrid part was produced using WAAM based on the GMAW process. First, the steel part was printed as a base structure with dimensions of 200 mm (length) × 30 mm (width) × 30 mm (height) using a linear bi-directional strategy with a 1.2 mm diameter wire. Subsequently, an NAB alloy was deposited on top of the steel substrate using a weaving deposition pattern. The bronze layers were also built with a 1.2 mm diameter wire and reached a final height of 20 mm. Tables 1 and 2 show the chemical composition of the wires and the processing parameters, respectively.

To analyse the microstructure, the sectioned surface was prepared using a standard metallography procedure for optical and scanning electron microscopy (SEM). Etching of the steel was performed using a solution composed of 100 mL ethanol, 5 mL hydrochloric acid, and 1 g of picric acid. For the NAB, an etchant consisting of 5 g ferric chloride, 25 mL hydrochloric acid, and 70 mL distilled water was employed. For EBSD measurements, the samples were further polished using OPS colloidal silica suspension. EBSD measurements were performed at an accelerating voltage of 20 kV with a beam spot size of 5 nm. A hexagonal scanning grid was used, with a step size ranging from 50 nm to 1 μm. The acquired data were subsequently processed using OIM Analysis™ software (version 9). The thin foils for transmission electron microscopy (TEM) were prepared by twin-jet electro-polishing using a 10 vol% $HClO_4$ + 90 vol% CH_3COOH solution.

Table 1
Nominal chemical composition (wt%) of the feedstock wires used for bimetallic printing.

	C	Si	Mn	Ni	Cr	Mo	Fe	Cu	Al
410 NiMo steel	0.01	0.65	0.7	4.8	12.2	0.5	Bal	<0.1	_
Bronze alloy	_	_	1.8	2.5	_	_	1.3	Bal	8.6

Table 2
Operating conditions used for manufacturing the bimetallic component.

	410 NiMo steel	Nickel-Aluminium Bronze
Current (A)	222	212
Voltage (V)	17.2	22
Travel Speed (mm/min)	650	1500-2500
Shield Gas and Flow (L/min)	Ar-35%He–2%CO_2 15	Ar-35%He 18
Layer Height (mm)	3	1.5
Hatch Spacing (mm)	5	-

The mechanical properties of the printed part were assessed through hardness measurements and tensile testing, supported by digital image correlation (DIC). For the hardness measurements, the Vickers hardness method was used with a load of 500 g and a dwell time of 10 s. Tensile test specimens were extracted along the building direction. Three sets of tensile samples were extracted: samples entirely from the steel part, samples entirely from the bronze part, and samples with the interface at the centre. The dimensions and extract location of the samples are shown in Fig. 1: (a) Dimension (in mm) and extract location of the tensile test samples All tensile tests were carried out at a strain rate of $\dot{\varepsilon} = 10^{-3}\ s^{-1}$ using a Deben testing machine, where the camera and DIC settings yielded a virtual gauge length, providing sufficient resolution for strain evaluation.

Additionally, a 2D DIC technique was used to evaluate the strain concentration of tensile test samples. Finally, the fracture surfaces of the tensile test samples were also studied using SEM.

3. Results

3.1. Microstructural analysis

Fig. 2 shows the printed part, in which the steel substrate and bronze deposition can be clearly discerned. In the following, the microstructure and mechanical properties in different regions of the fabricated part are further examined.

The optical micrograph in Fig. 3a illustrates the structure of the printed steel part. In this image, the melt pool structure is clearly visible, and fusion boundaries are indicated by white dashed lines. A closer examination of the microstructure is provided in Fig. 3b where within the melt pool, the microstructure appears coarse and elongated, whereas in the surrounding areas, a finer and more equiaxed structure is evident, which illustrates a certain degree of heterogeneity.

This indicates a certain degree of non-uniformity in the created structure. It is evident that the observed microstructure is the result of the repetitive formation of the melt pool microstructure and its surrounding areas, which reflects the additive nature of the manufacturing process. To better understand the differences in microstructural features and their development in the melt pool and HAZ, high-resolution EBSD (with step sizes of 100 and 50 nm) was performed, covering both regions. Figs. 4 and 5 show some of these results.

Fig. 4b and c shows the EBSD measured microstructure of the melt pool with an IPF and a grain boundary misorientation map, respectively. The latter reveals that 30% of the grain boundaries are Low Angle Grain Boundaries (LAGBs), indicating the presence of a martensite substructure. The grain size was measured as 13.39 ± 8.4 μm in this region. As HAGBs are predominantly oriented parallel to the BD, the structure

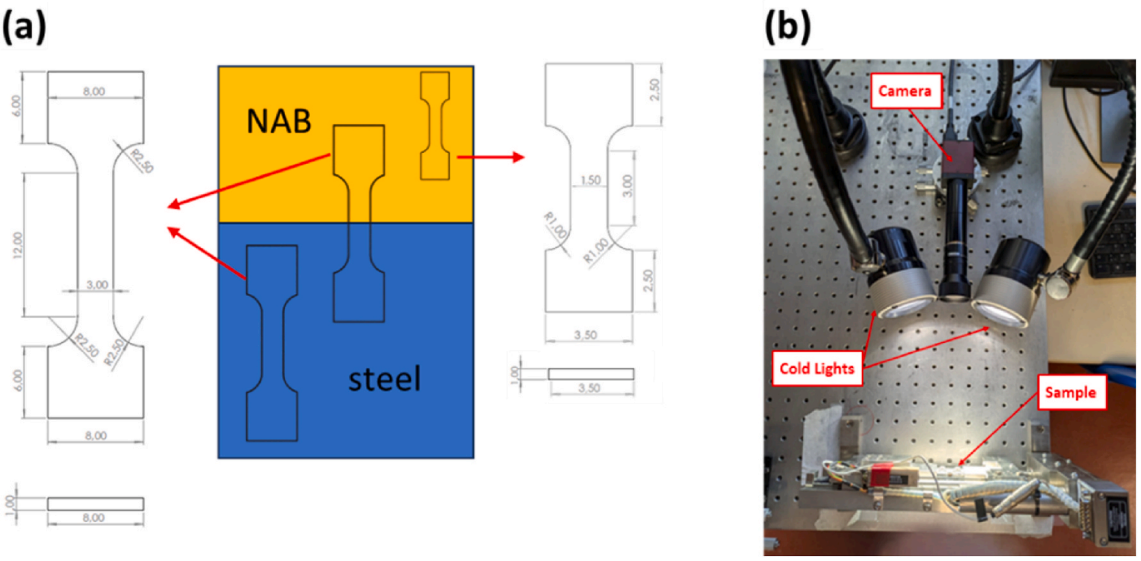


Fig. 1. (a) Dimension (in mm) and extract location of the tensile test samples, (b): The tensile test machine and DIC equipment.

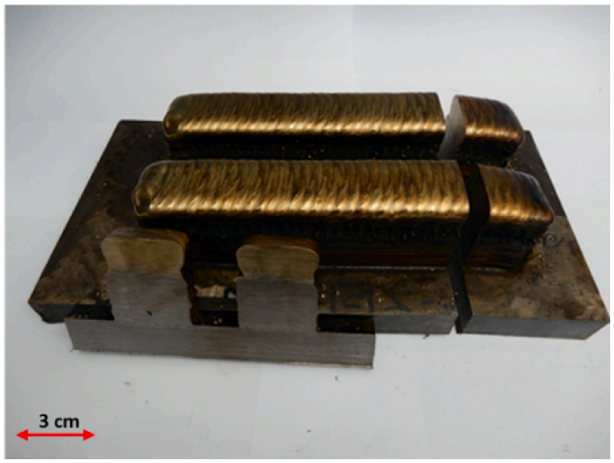


Fig. 2. The printed bimetallic part of NAB/SS.

exhibits an elongated morphology. To check the presence of retained austenite, a higher resolution scan (not shown here) with a step size of 50 nm was done inside the scan of Fig. 4b, and no austenite was observed in this region. Fig. 5b shows an SEM image of the microstructure within the melt pool, showing that, besides the martensitic structure, some δ-ferrite has also remained in the melt pool.

Continuation of the scan in Fig. 4b is shown in Fig. 4d and e. By going downward in the melt pool, it is observed that the lath morphology of the structure is decreased, and some equiaxed grains appear, see the bottom part of Fig. 4d. The grain size of the top and bottom regions of Fig. 4d was measured as 11.8 ± 3.8 μm and 8.17 ± 4.2 μm, respectively. Fig. 5c also shows the martensitic structure of this region. The changing size and shape of the grains in this region indicate some phase transformation during heating and cooling. A higher-resolution scan (not shown here) was also performed in this case, and no austenite was detected. No sign of delta ferrite was observed in this region. Fig. 4f and g shows the continuation of the EBSD scan from Fig. 4d. It is observed that the microstructure of this region is remarkably different, and the grain size in this region is decreased to 6.5 ± 6.2 μm. The presence of 3.5% retained austenite was also detected from the EBSD results. SEM images, Fig. 5d and e, reveal the presence of some fine grains of ferrite and some residual delta ferrite in this part of the HAZ. As the EBSD scan continued, cf. Fig. 4h and i, it is observed that the microstructure resembles the melt pool once more; however, Fig. 5f shows that the

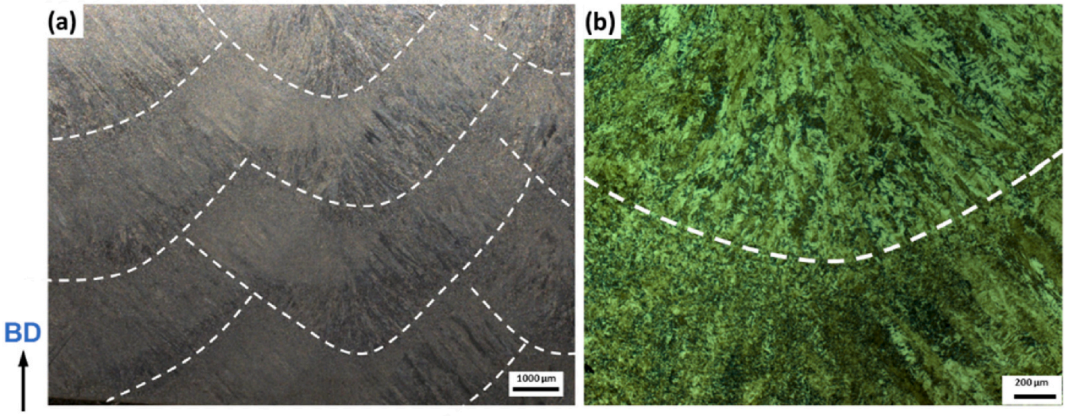


Fig. 3. (a) and (b), Optical micrograph of the microstructure of the printed steel part.

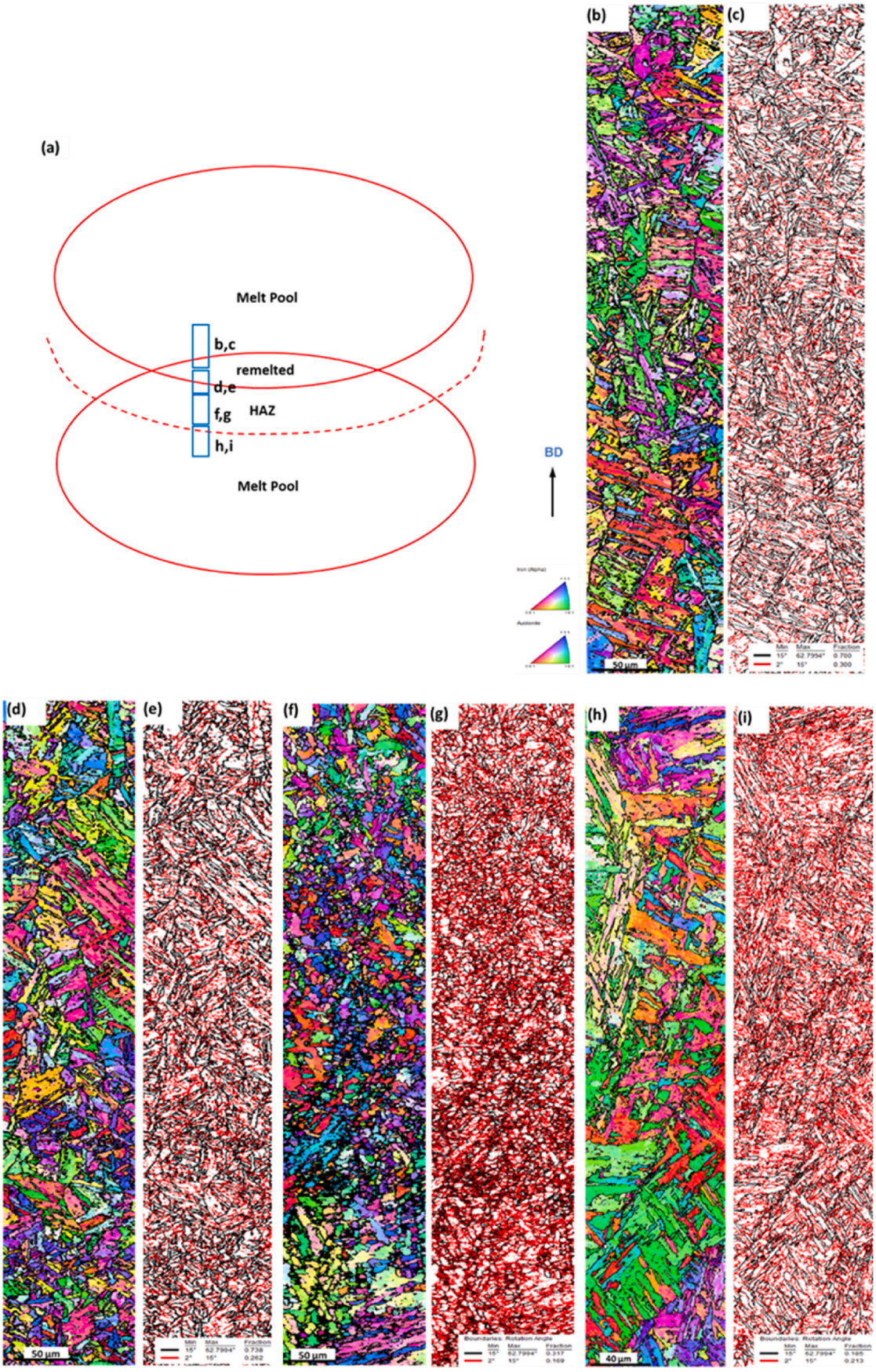


Fig. 4. EBSD maps showing a continuous scan from the melt pool through the HAZ (a): Schematic of the measured areas, (b) to (i), The scanning sequence progresses from (b) to (i) along the build direction (BD), capturing the microstructural transition across different regions. All IPFs are calculated based on BD.

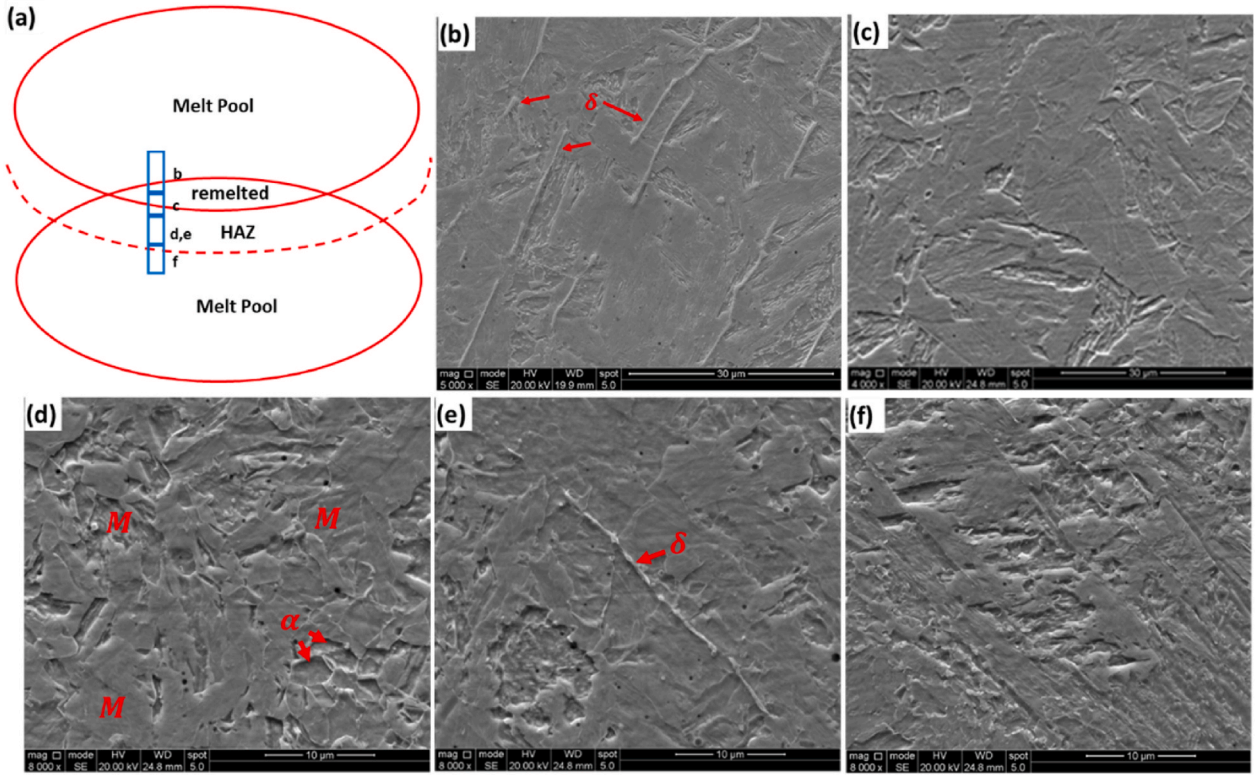


Fig. 5. The secondary electron-SEM images corresponding to different regions of the melt pool and HAZ.

martensite is slightly tempered. This zone is characterised by the absence of austenite formation during heating, and the precipitated carbides can be observed in the laths or at the prior austenite grain boundaries.

Fig. 6 shows the interface between the steel and bronze regions. It is observed that some cracks starting from the interface have developed toward the last deposited steel, cf. red arrow in Fig. 6a.

The EDS analysis shows the presence of a Cu-rich solidified liquid within the cracks, indicating the occurrence of Liquid Metal Embrittlement (LME). Fig. 7 shows the results of the TEM analysis of the sample extracted by FIB at the tip of the crack.

The TEM-EDS elemental maps reveal that the crack region is highly enriched in Cu, confirming that liquid bronze infiltrated the steel along the crack path. Interestingly, the Cu map also shows a low, but detectable, copper concentration in areas adjacent to the crack. This indicates that, in addition to crack-path infiltration, some Cu atoms have diffused into the nearby steel matrix during the high-temperature deposition process. Another notable observation is the presence of Al-rich particles near the crack tip. These particles display high Al concentration while showing relatively low levels of other alloying elements. Another interesting observation is that nearly all examined regions feature Cr-rich particles surrounding the crack, which appear as localized enrichments in the Cr map. This might be related to the presence of Cr-rich precipitates at grain boundaries prior to the occurrence of LME, and this segregation might alter grain boundary decohesion, thereby affecting crack propagation during the LME. There is no specific data on the Cu-Fe LME couple; however, studies [14,15] show that, in lead-induced LME in austenitic stainless steels, cracks usually follow paths containing impurities such as antimony (Sb), tin, or phosphorus (P). This can support the idea that, in a Cu-Fe LME couple, crack growth follows boundaries containing impurities or precipitates, such as Cr-rich ones.

Fig. 8 shows the microstructural features across the interface and Fig. 9 also shows the chemical analysis maps in this region. Just below the interface, a martensitic microstructure is observed on the steel side.

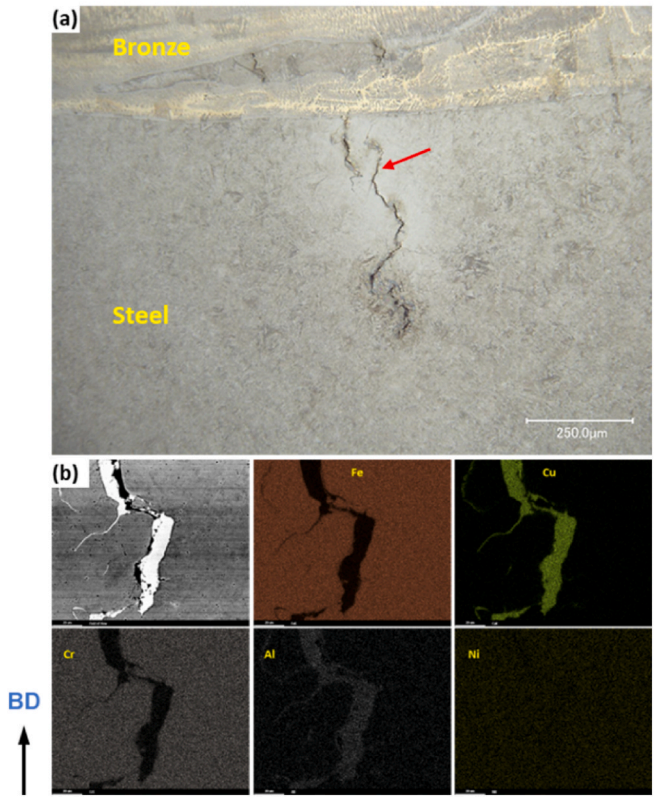


Fig. 6. The interface between steel and bronze parts (a): OM image, (b): back scatter image, as well as EDS analysis.

This is followed by a narrow interfacial layer, approximately 10–15 μm thick, above which a dendritic structure appears.

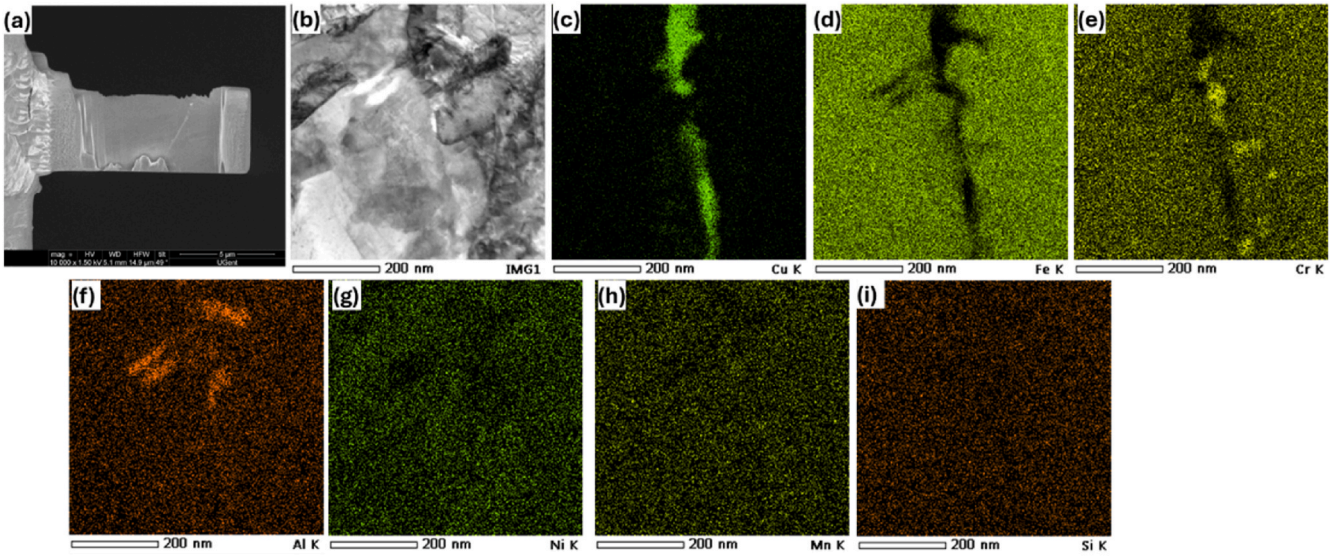


Fig. 7. TEM analysis of the crack tip (a): FIB sample (b): STEM image, (c-i): The EDS maps for different alloying elements.

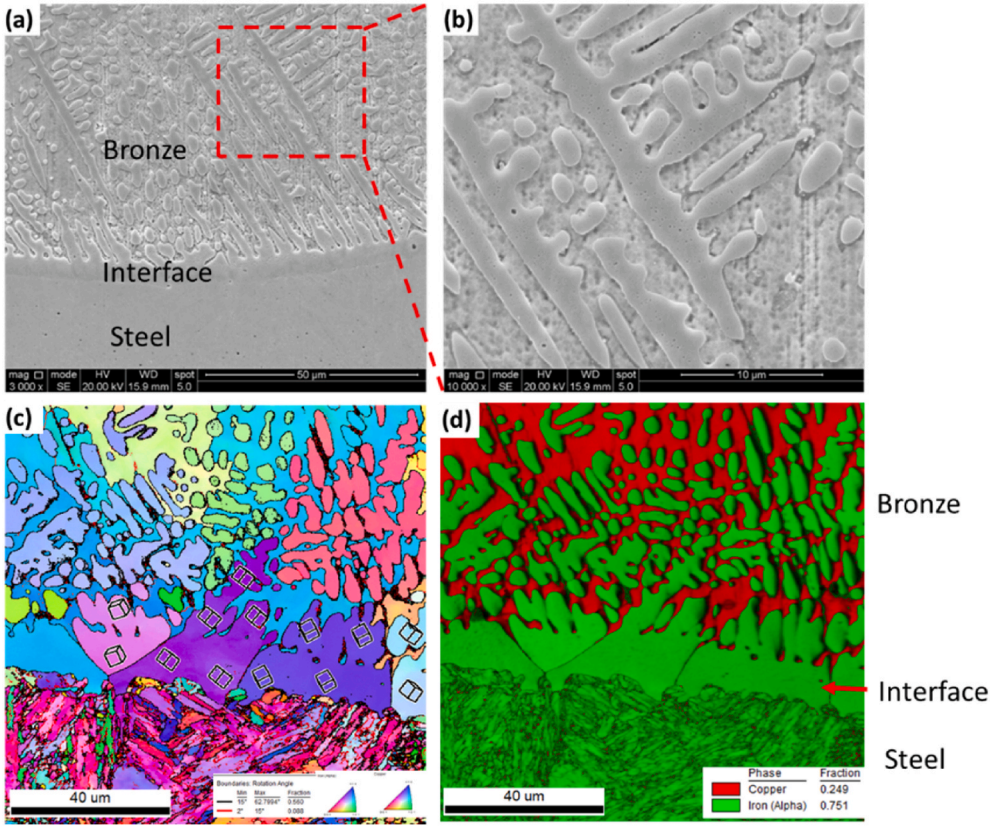


Fig. 8. Microstructure transition at the interface of steel and bronze (a) and (b): SE−SEM images, (c): BD-IPF image, (d): Phase map analysis, green BCC, red FCC. (For interpretation of the references to colour in this figure legend, the reader is referred to the Web version of this article.)

The interfacial layer, which is the first distinct feature observed above the steel region, exhibits a sharp interface with the martensitic steel layer. This layer has an average chemical composition (wt%) of Fe: 75.7, Cr: 13.6, Cu: 4.5, Ni: 3.3, Mn: 1.5, and Al: 1.1, indicating it is rich in Fe and likely formed as a transition zone between the steel and the overlay. The EBSD analysis also confirmed the BCC structure of this layer, cf. Fig. 8d. Above this interface layer, the microstructure consists of an FCC α- matrix with a composition of Fe: 16.3, Cr: 2.9, Cu: 75.4, Ni: 3.3, Mn: 1.4, and Al: 2.9 (wt%), containing a high volume fraction of Fe-rich columnar-dendrites. These large dendrites, known as k_I [16], which grow in the direction of the build, i.e. the maximum temperature gradient, exhibit an average composition of Fe: 72.4, Cr: 11.5, Cu: 6.5, Ni: 3.4, Mn: 1.7, and Al: 2.4 (wt%).

As shown in Fig. 8c, the columnar-dendritic structure originates from the interfacial layer and exhibits the same crystallographic orientation. This crystallographic continuity was confirmed by superimposing wire-

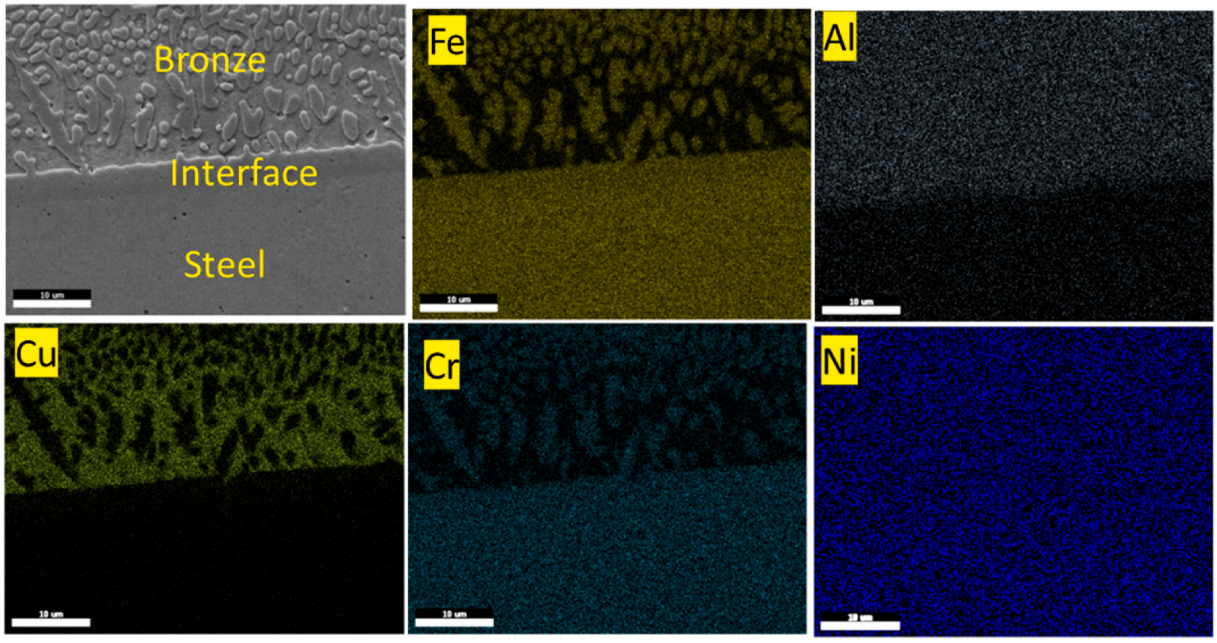


Fig. 9. The EDS chemical analysis across the interface of the bimetallic sample.

frame crystal representations on the EBSD map. The analysis reveals that the roots of the primary dendrite arms are located within the thin interfacial layer, from which they grow epitaxially along the building direction (BD). The matrix surrounding the dendritic structure reveals a face-centred cubic (FCC) structure, cf. Fig. 8d. Quantitative analysis indicates that the k_I phase represents approximately 29% of the overall microstructure of the bronze deposition.

As the distance from the interface increases, a transition in the microstructure is observed, as illustrated in Fig. 10. The initially large, columnar-dendritic structures are progressively replaced by smaller, globular and more equiaxed features of k_{II} phase [17] [18], with an average composition of Fe: 71.1, Cr: 0.4, Cu: 8.4, Ni: 2.9, Mn: 2.1, and Al: 4.1 (wt%), cf.Fig. 10b. These structures are embedded within an FCC matrix exhibiting a composition of Fe: 4.0, Cr: 10.6, Cu: 76.9, Ni: 3.3,

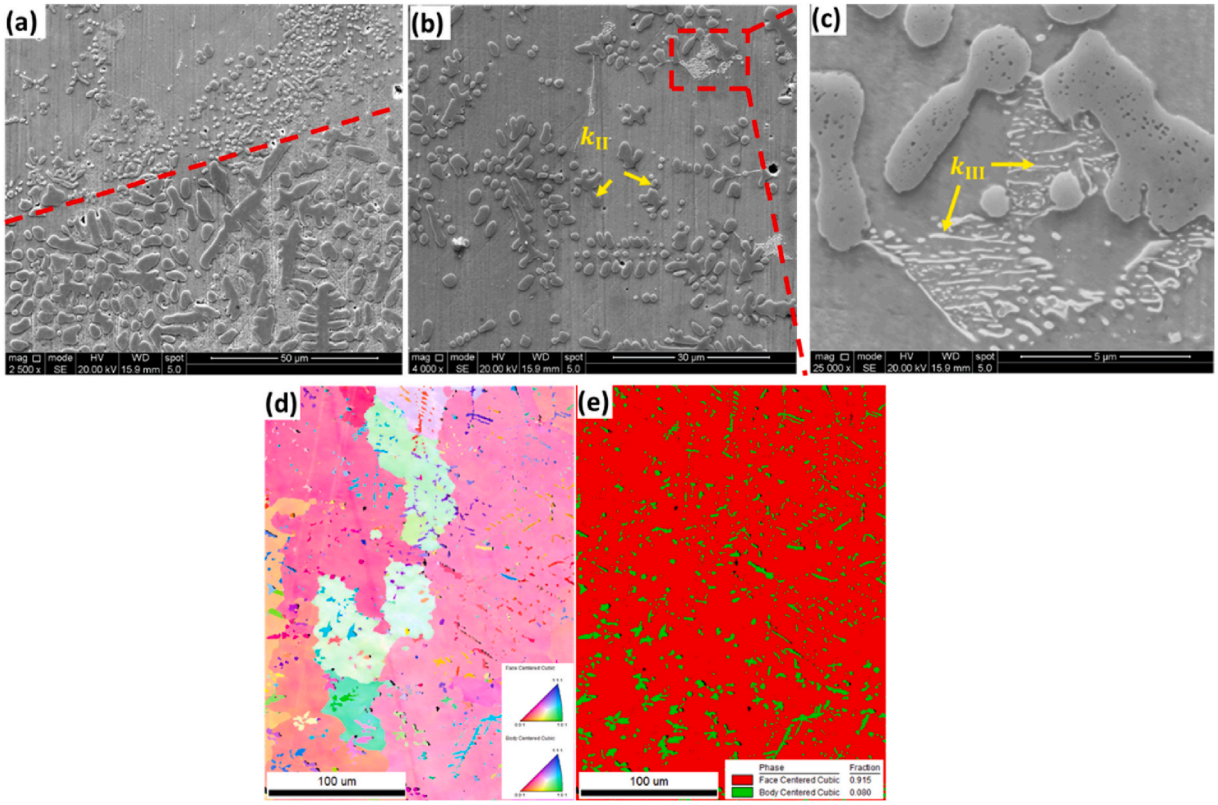


Fig. 10. The microstructure of the bronze part at the height of 1 mm from the interface (a): SEM image of the transition in microstructure (b) and (c): SEM images with higher magnification (d): BD-IPF image (e): phase analysis image.

Mn: 1.8, and Al: 3.4 (wt%). The literature reports that k_{II} is based on Fe_3Al whereby Ni, Cu and Mn substitute for iron [19]. Additionally, a eutectoid-like microstructure is observed in certain areas, cf. Fig. 10c, along with the presence of fine precipitates located at the grain boundaries of the α-matrix. This eutectoid feature is known as $\alpha + k_{III}$ mixture, which is formed from the reaction of $\beta \rightarrow \alpha + k_{III}$. The k_{III} is reported to be the intermetallic of NiAl [20] with minor solubility of Cu, Fe and Mn. It has been reported that by increasing the cooling rate, the temperature of the eutectoid reaction is decreased, resulting in a finer eutectoid microstructure [4]. The fraction of the BCC structure was measured to be 8% and reduced compared to the zone closer to the interface. The EDS map also confirmed the high concentration of Ni and Al in the region of this eutectoid mixture. The grain size of the FCC matrix was measured as 159.6 ± 81.6 μm.

At a larger distance of the interface in the bronze part, it is observed that the microstructure will also change. Fig. 11 shows the microstructure at a distance of 3.8 mm from the interface. It is observed that the grain size of the matrix is refined compared to the region just above the interface, exhibiting an average grain diameter of 28 ± 14 μm. The fraction of BCC phases has also decreased to 3%. In this region, the microstructure consists of α-dendrite, globular k_{II} and lamellar k_{III} phases. Fig. 11d shows the microstructure with higher resolution. It is seen that very fine precipitates have formed within the α-dendrites. These fine precipitates are known as k_{IV} phase. Some remaining β phases were also observed at grain boundaries as well as some twin boundaries. The presence of these twin boundaries is attributed to recrystallisation occurring during the deposition of the copper alloy. The high residual stresses can lead to localized plastic deformation, while the repeated thermal cycles from subsequent layer deposition act as a form of heat treatment, promoting recrystallisation.

At a distance of 4 to 5 mm from the interface, the microstructure is somewhat stabilized and remains stationary. Fig. 12 shows the microstructure of the last deposited layer, revealing that coarse grains of α-phase with a Widmanstätten morphology are the dominant structure. Moreover, some retained β and k_{III} phases are seen within the microstructure.

The EDS analysis also confirmed the enrichment of β regions with Ni and Al, cf. Fig. 12d.

3.2. Texture development

To analyse the crystallographic texture in the manufactured structure, the EBSD data were analysed. Fig. 13a shows an EBSD map in the middle height of the steel part. In this figure, the distinct microstructures of the melt pool and HAZ are clearly visible. The relevant pole figures, cf. Fig. 13b, show that this microstructural site exhibits a weakened texture. This is probably because of the successive solid-state phase transformations between high temperature and low temperature phases occurring during cooling of the steel structure.

Fig. 14 shows crystallographic texture analysis of two sequential layers in the NAB deposition. Fig. 14a presents the BD-IPF map, illustrating distinct crystallographic orientations between the top and bottom layers. The bottom layer is predominantly characterized by green colour, indicating a dominant <110>//BD orientation, whereas the top layer exhibits a more heterogeneous and multi-colored pattern, reflecting a wider range of orientations.

Fig. 14b and c provide the corresponding PFs and IPFs for the top and underlying layers, respectively. In the top layer, Fig. 14b, the PFs show nearly uniform intensity distributions, with a maximum pole density of only ~2, indicating a weak or nearly random crystallographic texture.

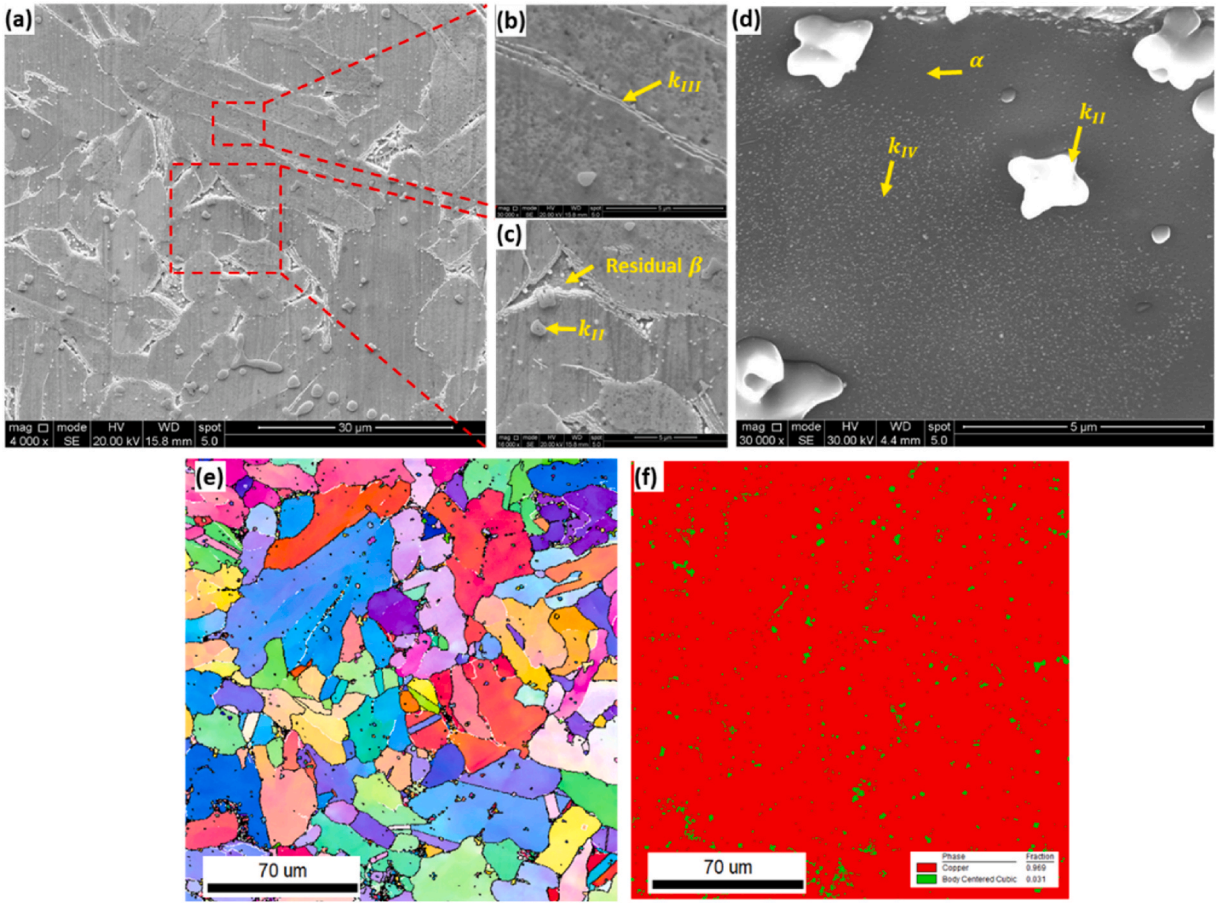


Fig. 11. The microstructure at a height of 3.8 mm from the interface (a), (b), (c), (d): SEM images (e) BD-IPF image (f): Phase map results.

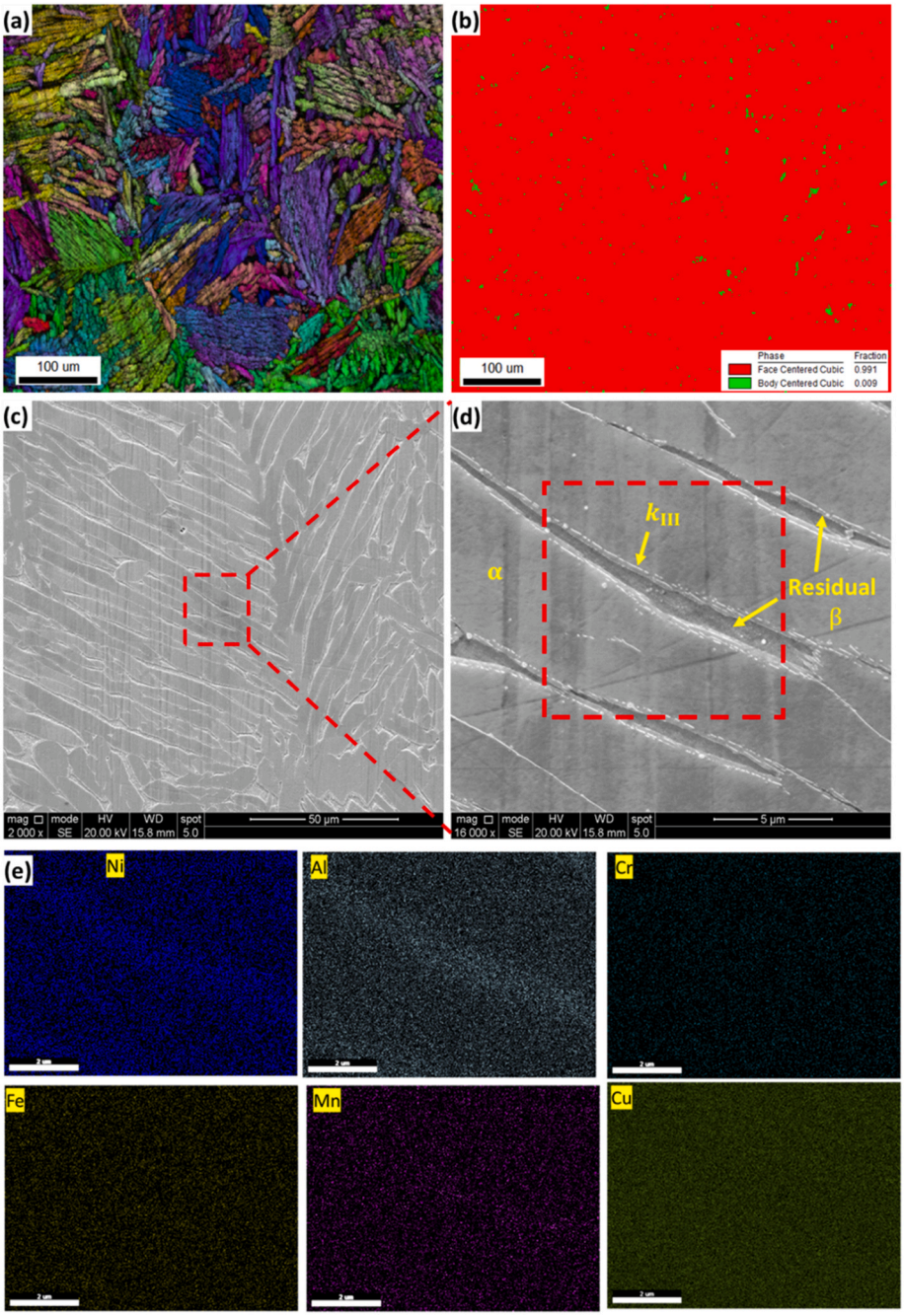


Fig. 12. The microstructure of the last deposited layer of bronze. (a): BD-IPF image (b): phase analysis image (c) and (d): SE−SEM images (e) EDS analysis of the area which is defined in (d).

The IPFs further support this, revealing no dominant crystallographic orientation along any of the three principal directions.

In contrast, the underlying layer, Fig. 14c, exhibits a noticeably stronger texture, with a maximum pole density of ~6.6. The PFs show preferential alignment of <101> and to a lesser extent <111> directions with the BD, whereas the <111> direction is aligned with WD. The IPFs confirm a more pronounced fiber texture, with grains preferentially oriented along <101>//BD and <111>//WD.

3.3. Mechanical properties

Fig. 15 shows the microhardness measurement results across the bimetallic interface.

On the steel side, the hardness value fluctuates between 340 and 380 HV. This fluctuation continues up to approximately 5 mm from the interface. These variations in hardness are attributed to the presence of distinct microstructural zones, such as the melt pool and HAZ. In the final two deposited steel layers, the hardness drops to a stable value of 350 HV. At the interface, a sharp drop in hardness is observed, from approximately 350 HV to 250 HV. Moving further into the NAB region, the hardness continues to decline, reaching a minimum of around 170 HV at ~16 mm from the sharp interface. This is followed by a slight increase to approximately 220 HV, after which a gradual decrease in hardness is observed toward the final deposited layers. The decrease in hardness in the NAB after the interface is attributed to a lower level of iron-rich constituents.

Fig. 16 and Table 3 present the engineering stress–strain curves and the corresponding tensile properties obtained from uniaxial tensile

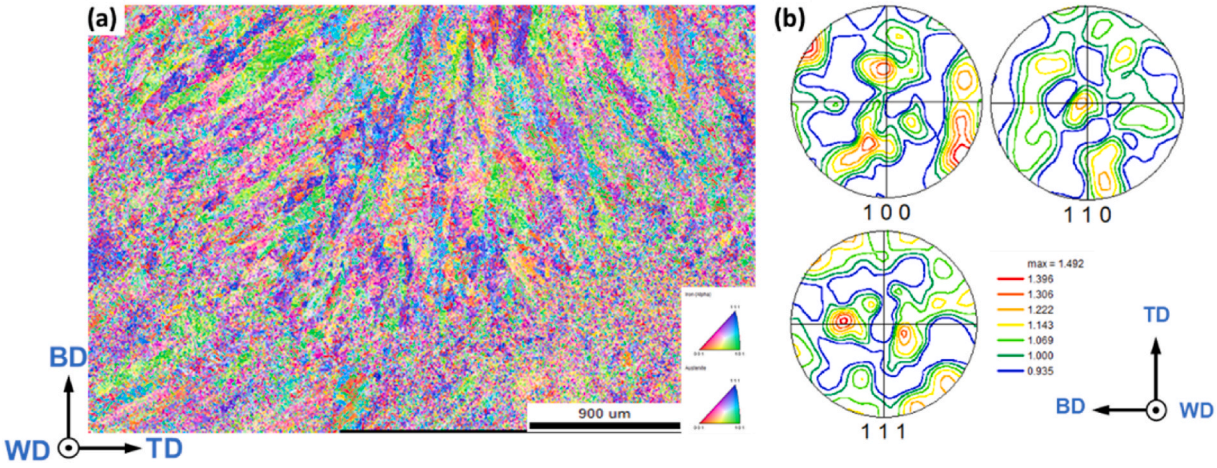


Fig. 13. (a): BD-IPF map of a melt pool and surrounding area in the steel part at a height of 16 mm from the substrate, (b): The relevant PFs.

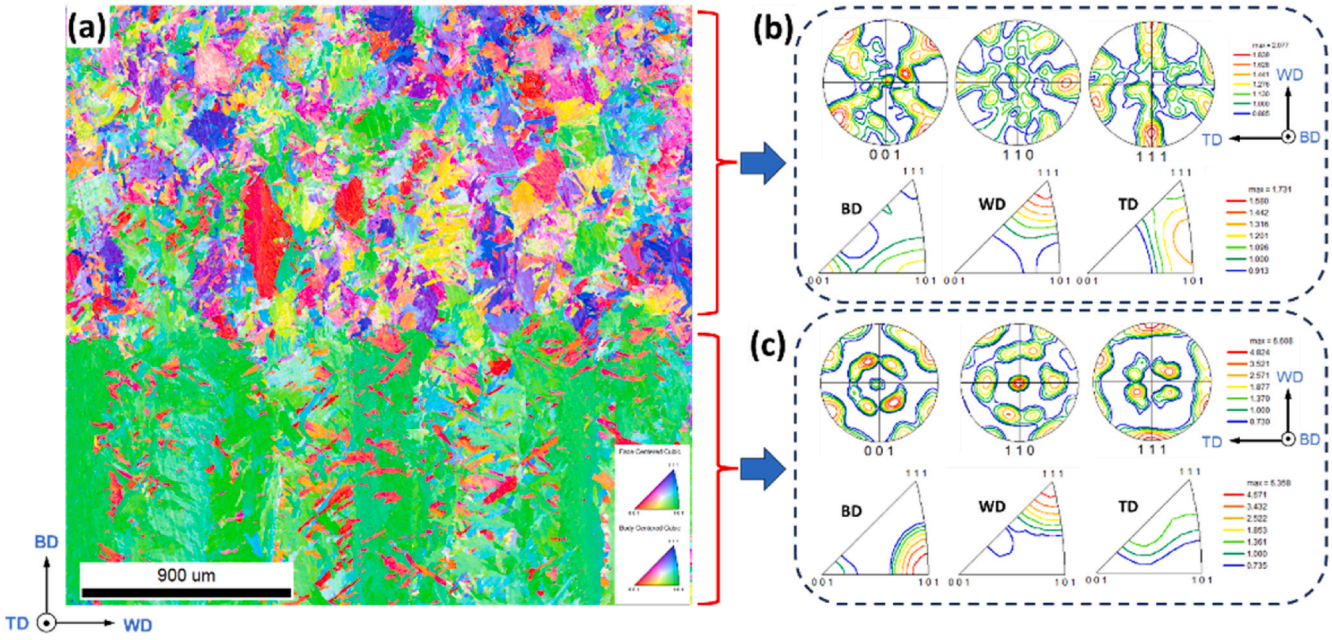


Fig. 14. (a): BD-IPF map of the bronze side at a height of 17 mm from the interface (b): The relevant PFs.

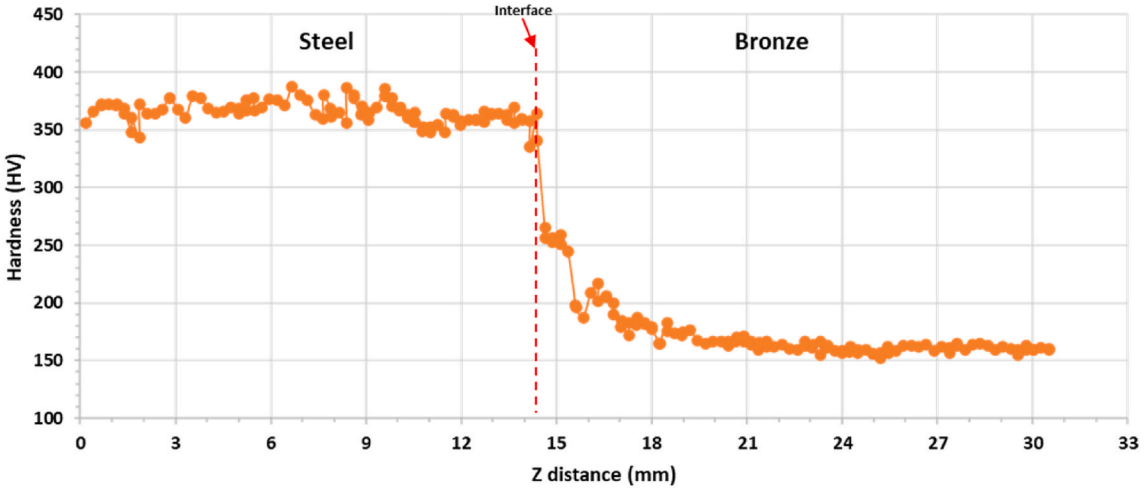


Fig. 15. The hardness variation across the interface of the bimetallic structure.

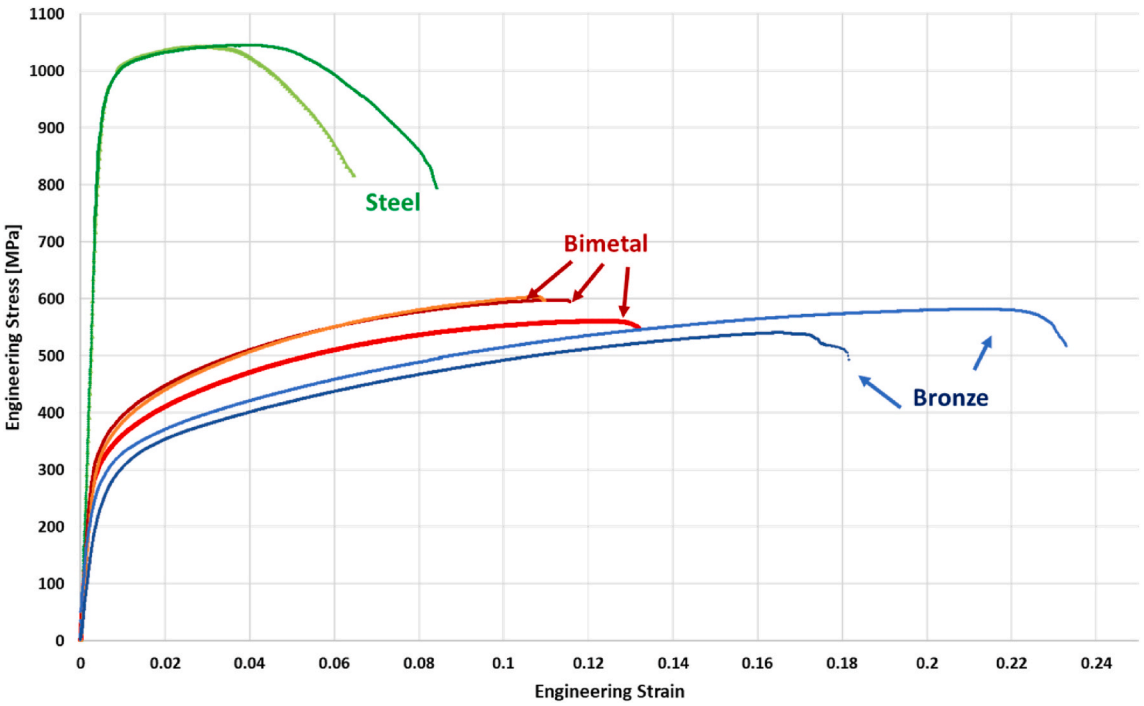


Fig. 16. The stress - strain behaviour obtained from tensile tests of steel, bronze and bimetallic samples.

Table 3
The mechanical properties derived from the tensile test measurements.

Material	UTS (MPa)	Uniform Elongation (%)	Total Elongation (%)
Steel	1045 ± 7	4 ± 0.5	7.4 ± 1.4
NAB alloy	561 ± 29	19.2 ± 3.6	20.8 ± 3.6
Bimetal	587 ± 23	11.7 ± 0.8	12 ± 1.2

testing. It should be noted that the NAB region exhibits a pronounced microstructural gradient along the build direction. Therefore, the tensile properties reported in Fig. 16 represent an effective macroscopic response of the NAB material observed macroscopically in a defined region of the build, rather than a spatially resolved assessment of each microstructural zone. As such, the measured strength and ductility reflect an average homogenized response that integrates contributions from different κ-phase populations and matrix morphologies within the gauge length. It is important to note that the NAB tensile specimens were obtained from the upper section of the NAB build, positioned several millimeters away from the steel–NAB interface. In this region, the microstructure had stabilized and dilution effects from the steel substrate were minimal.

The steel and NAB samples exhibited ultimate tensile strengths (UTS) of 1045 ± 7 MPa and 561 ± 29 MPa, respectively. The total elongation at fracture was 7.4 ± 1.4% for the steel and 20.8 ± 3.6% for the NAB specimens.

The steel samples also exhibited pronounced necking before fracture, indicating a high degree of localized plastic deformation after the onset of necking. Such necking stability is not common in martensitic stainless steels, which are typically characterised by limited ductility and early fracture. The presence of retained austenite, which was quantified by EBSD, may contribute to sustained work hardening during tensile deformation via a TRIP-assisted mechanism, thereby delaying strain localization and localized necking. However, it should be noted that the rather small fraction of retained austenite (~3.5%) cannot provide a dominant contribution to work hardening through a TRIP-assisted mechanism. Instead, the observed behavior can also be attributed to the microstructural heterogeneity introduced by the WAAM process, including variations in grain morphology and phase distribution. These heterogeneities can promote strain partitioning and progressive plastic deformation, thereby delaying strain localization and enhancing necking stability. The bimetallic sample demonstrated a UTS of 587 ± 23 MPa and a total elongation of 12 ± 1.2%, indicating its mechanical performance lies between that of the steel and NAB materials. The extended post-necking deformation was not observed in NAB or the bimetallic samples. In the bimetallic samples, it was observed that the failure location is always on the bronze side. To gain a better understanding of the deformation process, DIC was also conducted during tensile tests of which the results are summarised in Fig. 17.

For the steel sample, Fig. 17a, the evaluation of the strain field, in the X direction, begins with an initially uniform distribution across the gauge length. As the loading progresses, the strain starts to concentrate in certain bands. With further increasing load, the higher concentration occurs in one of these bands, and ultimately, fracture occurs in that band. The strain concentration in bands is observed in those bands until the fracture. For NAB samples, Fig. 17b, strain is started in a uniform manner, and as deformation proceeds, a gradual increase in strain concentration is observed along the gauge section. Unlike the steel samples, this specimen exhibits a more diffuse strain localization over a broader zone before necking fully develops. The peak strain for the NAB sample was 0.7, which is higher than that observed for the steel sample, indicating higher plastic deformation before fracture. For the bimetallic samples (Fig. 17c), the strain initially remains uniformly low throughout both the steel and NAB regions, points 1 and 2 on the stress-strain curve. As loading increases, strain localization begins in the softer bronze section, while the steel region shows limited deformation, point 3. At higher strains, points 4 and 5, the bronze undergoes significant plastic deformation, with the strain concentrating near the upper gauge length, while the interface does not fail. The final frame shows that failure initiates in the bronze region, well away from the interface at the beginning of the stabilized NAB zone, where the microstructure is dominated by Widmanstätten morphology, suggesting efficient load transfer across the interface of dissimilar materials under the uniaxial loading conditions.

Fig. 18 shows the fractography of the fracture surfaces of the tensile test samples. The steel fracture surfaces, Fig. 18a–c, display a ductile

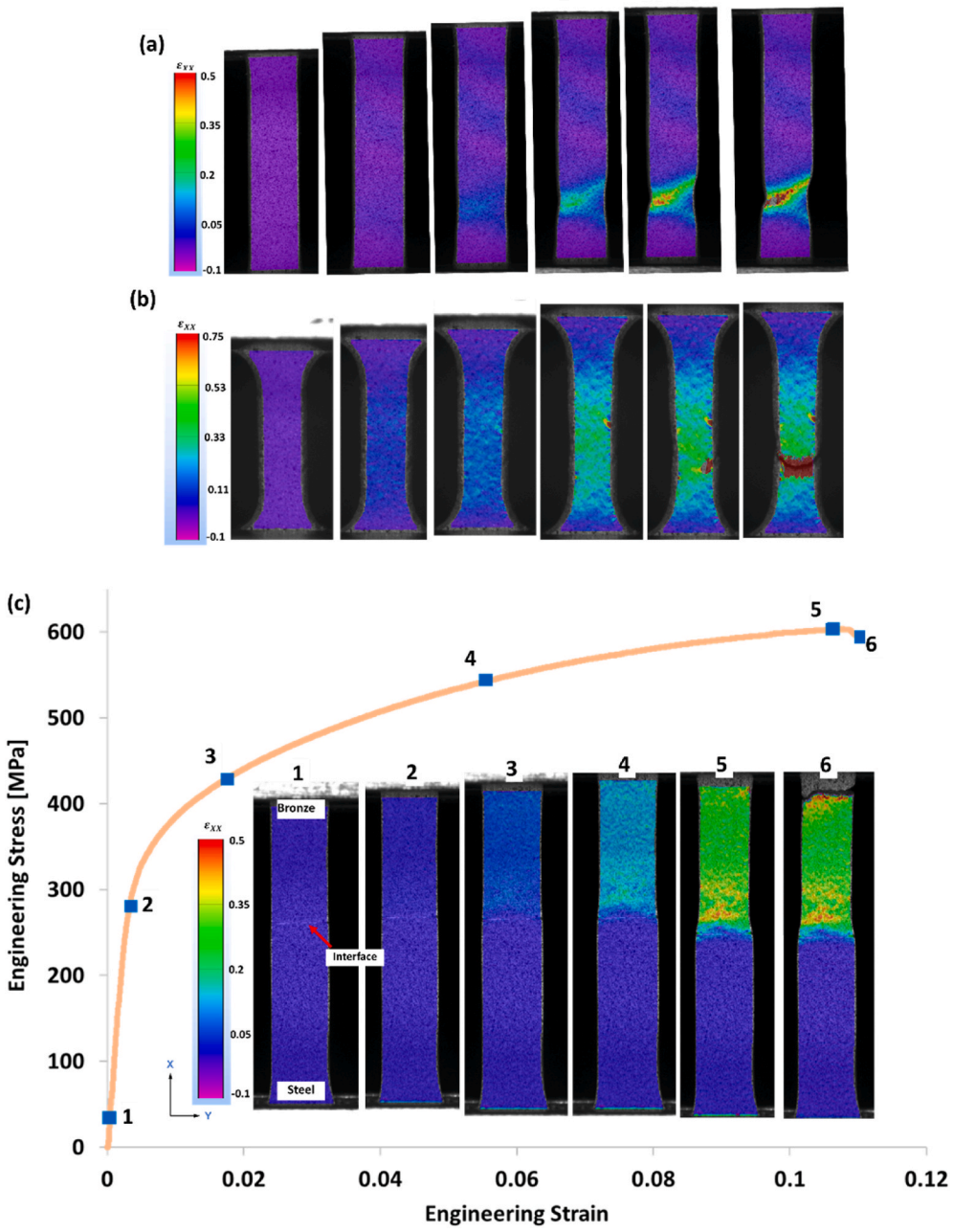


Fig. 17. The DIC results for tensile test samples, (a): Steel, (b): NAB and (c): Bimetallic sample.

fracture mode, with conical equiaxed and fine dimples covering the surface. This indicates the formation and coalescence of microvoids.

In the NAB, the fracture surfaces (Fig. 18d–f) also exhibit areas covered with dimples. Besides dimples, smooth facets perpendicular to the tensile direction (highlighted by red arrows), which are surrounded by tear ridges (yellow arrows), are also visible on the surface, indicating the brittle fracture. Additionally, some microcracks are also observed in the facets (green arrows). These cracks are formed after passing the main cracks during fracture, and are considered secondary cracks. The presence of secondary cracks is another feature of brittle fracture. It has been reported that in NAB alloys, they occur at the boundary between α grains and lamellar eutectoid structure ($\alpha + K_{III}$) and propagate along phase interfaces [21]. In the bimetallic sample (Fig. 18g–i), the fracture surface morphology closely resembles that of the NAB sample; however, qualitative observations show a greater presence of brittle features, suggesting a higher contribution of brittle fracture during tensile loading. This may be related to the distinct microstructural context at the fracture location. In the bimetallic specimen, fracture initiation occurred at the onset of the stabilized NAB region, whereas in the monolithic NAB sample it occurred at higher build heights within a more uniformly stabilized microstructure. Consequently, the NAB region involved in fracture in the bimetallic sample contains a higher fraction of intermetallic and secondary phases, in addition to the FCC Cu-based matrix. The presence of these harder, less deformable phases promotes local strain localization and early damage initiation, which can reduce the extent of ductile deformation and result in a higher proportion of brittle-appearing features on the fracture surface than in the monolithic NAB sample.

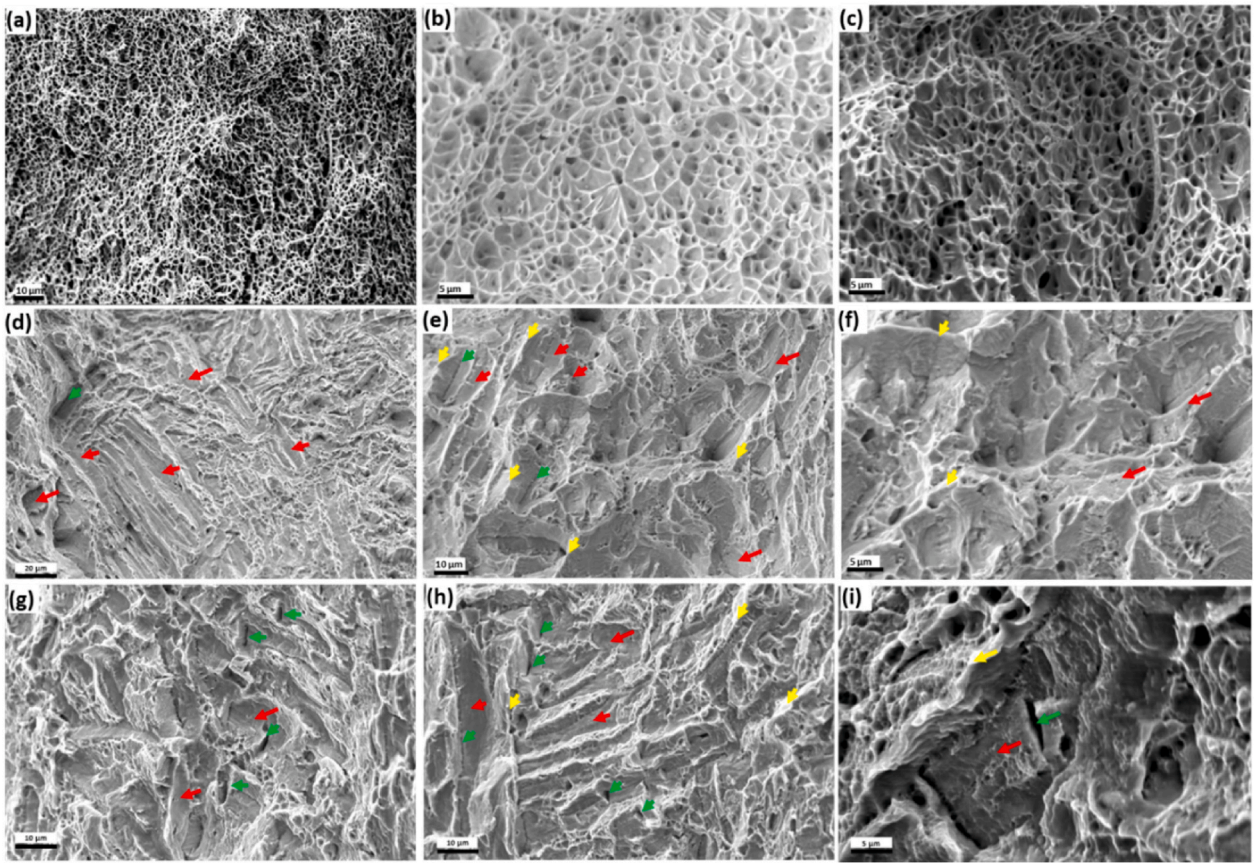


Fig. 18. The SEM images of the fracture morphologies of tensile test samples, (a), (b), (c): steel samples, (d), (e), (f): NAB sample and (g), (h), (i): bimetalllic sample.

4. Discussion

4.1. Microstructure formation

Although detailed thermal history data (e.g., in situ temperature measurements or modeled heating and cooling rates) were not acquired in this study, the microstructural evolution is interpreted in the context of the characteristic thermal cycling inherent to the WAAM process. WAAM is known to involve repeated heating and cooling cycles, steep thermal gradients, and non-equilibrium solidification, which strongly influence phase formation, grain morphology, and elemental redistribution. The discussion, therefore, focuses on correlating the observed microstructural trends with these established thermal characteristics rather than with explicitly measured thermal histories.

4.1.1. Stainless steel side

The microstructure of the 410 NiMo stainless steel part shows a predominant martensitic structure along with other phases such as δ-ferrite, α-ferrite, and retained austenite. The microstructure of the melt pool was identified as martensite and retained δ-ferrite, cf. Fig. 4a, b and i. The development of this microstructure relates to solidification and solid-state phase transformations occurring in this region. The transformation path for the melt pool is as follows:

$$L \rightarrow L+\delta\,(ferrite) \rightarrow \delta \rightarrow \delta+\gamma\,(austenite) \rightarrow \delta + M(martensite) \quad (1)$$

The melt pool solidifies as δ-ferrite, and by the end of solidification, the microstructure is entirely δ-ferrite. With further cooling in the solid state, the δ-ferrite transforms into austenite, which then converts to martensite upon additional cooling. Notably, some parts of the δ-ferrite phase formed at the end of solidification may be enriched with ferrite-stabilising elements like Cr and Mo. Consequently, this ferrite does not transform into austenite during cooling and remains present in the final microstructure alongside martensite. Therefore, the final microstructure of the melt pool consists of martensite and δ-ferrite, as observed in Fig. 4b and c. Other researchers [22] [23] [24] have also reported such microstructure during the additive manufacturing of 410 stainless steel.

The material surrounding the melt pool, i.e. the HAZ, experiences only heating and cooling cycles. Depending on the peak temperatures reached in various sub-regions, different microstructures may develop. The initial microstructure in this region is the melt pool, which consists of martensite and retained δ-ferrite. When the temperature exceeds the ferritization temperature (Ac_4), δ-ferrite forms during heating. At such high temperatures (1230°C for the proposed steel), diffusion is sufficiently enhanced, even if the exposure time is short, to dissolve the initial δ-ferrite. This explains the absence of δ-ferrite in the microstructure of this region [25]. So, the retained δ-ferrite in the initial microstructure dissolves, and upon cooling, austenite forms. With further cooling, the microstructure becomes fully martensitic (cf. Fig. 4d and e). Another notable point is that the cooling rate in the HAZ is significantly lower than in the melt pool, allowing sufficient time for δ-ferrite to transform into ferrite during cooling.

If the peak temperature is not sufficient for ferritisation but is higher than austenisation (approximately 730 °C), austenite forms during heating and, after cooling, transforms into martensite. When partial austenisation occurs, α-ferrite also forms during heating together with austenite and remains in the microstructure after cooling, cf. Fig. 4f and g. Additionally, in these regions, the temperature and time conditions are not high enough to dissolve the initial δ-ferrite, so it remains in the microstructure. If the temperature is below austenisation, no austenite forms, and only the initial microstructure experiences tempering, resulting in tempered martensite and residual δ-ferrite.

One interesting aspect of the steel microstructure is the lack of coarse-grained structures in HAZ, which are often seen during the welding of this group of steels [26]. One reason may be the presence of

inclusions in the microstructure of printed steel, arising from undesirable chemical reactions in the melt pool. To investigate this hypothesis, TEM analysis was performed on steel samples, as shown in Fig. 19. The chemical analysis revealed the presence of fine silicon and manganese oxide particles, which result from the oxidation during WAAM. These oxide particles serve as barriers that pin the grain boundaries, preventing their movement and suppressing grain growth, ultimately leading to a fine-grained microstructure [27,28].

4.1.2. Interface and NAB side

The microstructure of NAB alloys depends on their chemical composition and the thermal path experienced during cooling. The solidification of the proposed NAB alloy starts with the solidification of α dendrites from the liquid. Then, at the temperature of 1030 °C, a portion of the α-phase experiences the peritectic reaction of $L+\alpha \rightarrow \beta$ to form the β phase in interdendritic regions. Because of the high tendency of alloying elements to segregate into the liquid, especially Fe, the last portion of liquid which solidifies has a higher level of alloying elements. This can cause the formation of large and rossette-like k_I particles, which are based on Fe_3Al, in interdendritic regions. It is noticeable that at high cooling rates, the segregation of elements will be restricted and the formation of the k_I phase is suppressed. This is the reason that researchers have reported the absence of k_I phases in the microstructure of additively manufactured NAB alloys [29] [30].

After solidification, the alloy undergoes solid-state phase transformations upon cooling, the first of which is entering the α + β region. In this region, the k_{II} phase is formed at the interface of α and β during cooling. Like k_I, the k_{II} phase is also based on Fe_3Al, but its particle size is smaller.

After that, at temperatures around 800 °C, the eutectoid reaction of $\beta \rightarrow \alpha + k_{III}$ consumes the β phase. This results in the formation of a lamellar structure of k_{III} + α in interdendritic regions where the initial β was present. The k_{III} phase is a Ni-rich phase based on NiAl. If the cooling rate is high, then not all the β experiences the eutectic reaction, and some of it remains in the microstructure.

Finally, upon further cooling, fine k_{IV} phase particles precipitate and become uniformly dispersed within the primary α dendrites. The k_{IV} phase is based on Fe_3Al and are formed as the solubility of iron in α is exceeded. They precipitate at the center of the α grains, as this region remains unaffected by local iron depletion associated with the formation of k_I or k_{II} phases.

In WAAM, cooling rates are high enough to suppress high-temperature k_I precipitation but insufficient to fully inhibit k_{II}, k_{III}, and k_{IV} formation. As cooling rate slows with decreasing temperature, intermediate-temperature precipitations are more likely to occur. Therefore, k_{II-IV} phases still form via solid-state transformations in WAAM-NAB.

Accordingly, the microstructure of the proposed NAB alloy is generally expected to comprise α-phase grains accompanied by various K phase precipitates. However, due to complex thermal cycling accompanied by WAAM and local variations in chemical composition arising from dilution effects, the resulting microstructure exhibits spatial heterogeneity. It is notable that the κ-phases in NAB alloys are ordered intermetallics derived from the BCC lattice (e.g., B2 or DO_3 structures); however, due to their similar crystal symmetry and the limited sensitivity of conventional EBSD, a clear crystallographic distinction between individual κ-phase types cannot be reliably established using EBSD alone. So, in the present study, κ-phases were primarily distinguished by their morphology, size, spatial distribution, and region of formation.

During deposition of the first NAB layer on the steel substrate, a portion of the substrate remelts and mixes with the molten NAB. The complex interaction involving melting, mixing, diffusion and solidification under non-equilibrium conditions governs the formation of the interface between NAB and SS. Considering the binary phase diagram of Cu-Fe, there is a miscibility gap, which implies that the Fe-Cu liquid separates in an Fe-rich and a Cu-rich liquid during cooling [31]. Accordingly, it is logical to consider that the liquid containing NAB and SS undergoes a liquid separation during cooling. Another factor that can corroborate the separation of SS and NAB is the different surface tensions of the SS and NAB phases. Additionally, this is intensified by high cooling rates accompanied by additive manufacturing, especially at the bottom of the melt pool with increased cooling rate. It is noticeable that the separation of the Cu-rich and Fe-rich liquid phases does not preclude interfacial interaction between them. Even after phase separation, chemical exchange may occur before solidification, as evidenced by the presence of Cu and Al, originating from the NAB side, within the solidified interface layer. The incorporation of these elements cannot be solely attributed to post-solidification diffusion, indicating that interdiffusion between the immiscible liquid phases likely occurred before starting solidification. In fact, during mixing, both liquids can dissolve into each other, which results in the enrichment of the SS liquid with Cu and Al, while the NAB liquid dissolves Fe, Cr, and Ni from SS. Given the higher melting point of stainless steel (Fe-rich phase) compared to NAB (Cu-rich phase), the Fe-rich dendrites are the first to solidify from the melt. Subsequently, the Cu-rich NAB solidifies in the interdendritic regions. This explains the microstructural observation in the first deposited layer of NAB, cf. Fig. 8, where Fe-rich dendrites are embedded within a Cu-rich matrix occupying the interdendritic spaces.

Li et al. [17] have also reported the formation of such an interface and dendrites during printing a NAB alloy on top of 15-5 PH steel using laser-powder directed energy deposition whereby they showed the presence of Fe and Cr-rich phases. Hassan et al. [16] who studied the microstructure of NAB alloys, have reported the formation of large dendritic particles in the microstructure of as-cast NAB alloys that contain a high level of Fe. They also reported that these k_I dendrites contain small precipitates which are rich in Cu. To check this, the TEM analysis was done, which confirms the formation of these Cu-rich precipitates within k_I dendrites, cf. Fig. 20.

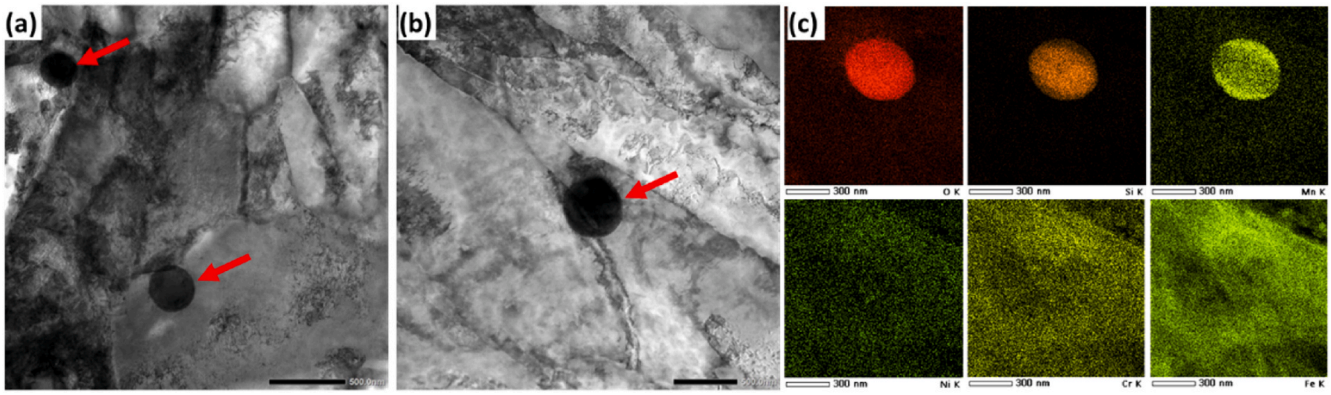


Fig. 19. (a) and (b): STEM images of inclusions formed within the microstructure of the steel part (c): Chemical analysis of inclusion particle in image (b).

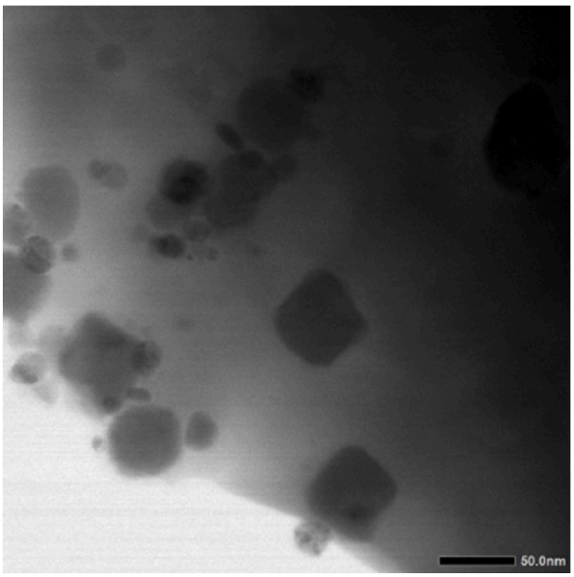


Fig. 20. STEM image of the microstructure of k_I dendrites in the first deposited layer of NAB, showing the formation of Cu-rich precipitates in k_I dendrites.

In the second and further deposited layers of bronze, the k_I phase is no longer observed; instead, other k phases emerge, cf. Figs. 10–9. The absence of the k_I phase is primarily attributed to the reduced Fe concentration in these layers, which results from decreased dilution effect [30]. In fact, the newly deposited NAB is mixed with a previously deposited substrate that is already diluted and thus contains lower amounts of stainless steel alloying elements. This leads to a gradual reduction in Fe and Cr concentrations in the matrix with increasing distance from the interface, thereby reducing the formation of the k_I phase.

In regions unaffected by dilution, about 4 mm away from the interface, the microstructure of the NAB layers begins to stabilize, exhibiting a Widmanstätten α structure accompanied by minor amounts of retained β phase, k_{III} and k_{IV} precipitates (cf. Fig. 12). Other researchers [32] [33] have also reported these microstructures during WAAM of NAB.

One interesting phenomenon observed in the microstructure of the NAB/SS bimetallic structure was the presence of LME. Other researchers have also observed the presence of LME cracks at the interface during the additive manufacturing of Cu alloys on top of stainless steels [34] [35]. The occurrence of LME results from the simultaneous presence of three factors: (i) an aggressive liquid, (ii) a susceptible solid, and (iii) tensile stresses [36]. In the present case, it occurs when the copper-based liquid in direct contact with the solid steel structure penetrates the grain boundaries of steel in the presence of tensile stresses. The authors have explored this phenomenon in this particular case, which can be found in Ref. [37].

4.2. Texture development

Texture analysis based on EBSD measurements revealed differences between the stainless steel (SS) and NAB regions. As shown in Fig. 13, the steel microstructure exhibits a weakened texture. This is primarily attributed to solid-state phase transformations occurring after solidification. Given that martensite constitutes the predominant microstructure in the steel region, reconstructing the prior austenite phase and analysing its texture is essential to better understand the texture evolution. The reconstruction was performed using the Greninger–Troiano (G–T) orientation relationship. This orientation relationship was chosen based on examination of the interfaces of retained austenite phases, which showed that most of them adhered to the G–T relationship. Fig. 21 presents the reconstructed austenitic microstructure together with its PFs. Notably, the austenitic structure also exhibits a weak texture. Considering the sequence of solid-state transformations, the δ-ferrite is formed as the primary solid phase, which subsequently transforms into austenite. This diffusive phase transformation can significantly alter or even destroy the initial texture established in the δ-ferrite phase.

For the NAB part, it was observed that some deposited layers have a textured microstructure. As the α phase is the primary phase that solidifies from liquid, and it remains in the microstructure till room temperature, it is expected that the final microstructure could have a textured microstructure. It is noticeable that the two analysed layers have almost the same microstructure predominantly consisting of Widmanstätten α as well as some K precipitates. However, it was observed that the last deposited layer has a weakened texture, while the next-to-last layer exhibits a strong <101>//BD texture. Development of the latter has been reported during AM of some metallic alloys [38] [39] [40]. During solidification, the grain orientations are selected based on the local thermal gradient. Accordingly, the shape (or geometry) of the melt pool is a determining factor for texture development during WAAM and also other AM processes. In the cases that deposition parameters result in a shape of the melt pool with a near semicircular cross section, substantial portions of the solid–liquid interface are oriented at angles of approximately 45° relative to the BD. This geometry favours the crystallographic orientations in which the <110> direction is aligned with BD [41].

The observed texture transition in the final deposited layer of NAB can be attributed to the distinct solidification conditions. The use of a

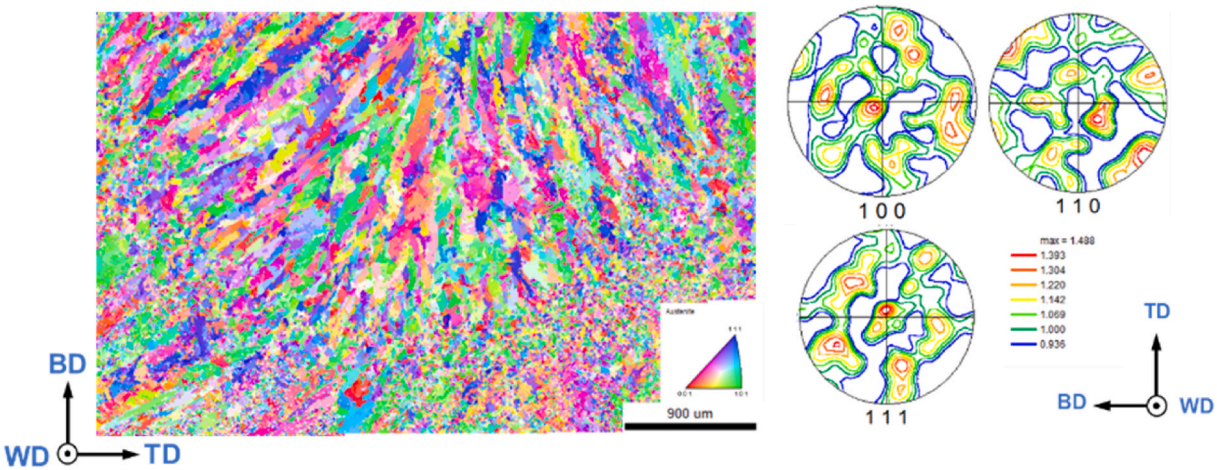


Fig. 21. Reconstructed austenite structure relevant to Fig. 13 and its corspodense PFs.

weaving deposition strategy introduces layer-to-layer variations in the scanning direction, which in turn alters the orientation of thermal gradients. As the deposition sequence progresses, the overall cooling rate tends to decrease, further modifying the local solidification dynamics. Additionally, unlike the layers beneath, the last layer does not experience any thermal cycle from the subsequent deposited layers above. These combined factors, reduced cooling rate, absence of overlying heat input, and directional changes in scanning, can promote a shift from a more equiaxed dendritic morphology that influences the crystallographic texture, thereby producing the distinct texture evolution evident in the final layer, as illustrated in Fig. 14. The potential influence of the observed fiber texture on the anisotropy of mechanical behavior requires further investigation.

4.3. Mechanical properties

The hardness gradient observed across the NAB region (Fig. 15) can be understood by considering the combined microstructural features. In the region immediately following the interface (Fig. 9), the microstructure is strongly influenced by dilution and contains a relatively high fraction of k_I phase embedded in a Cu-based FCC matrix. Due to dilution, the FCC matrix is highly alloyed, thereby increasing its hardness through solid-solution strengthening. The combined presence of hard k_I phases and a strongly alloyed FCC matrix therefore accounts for the higher hardness observed in this region. With increasing the distance from the interface, the total fraction of k phases is decreased as a result of the reduced Fe content associated with the diminishing dilution effect. In addition, the concentration of alloying elements in the FCC matrix decreases, and the matrix composition approaches that of the nominal NAB, resulting in reduced solid-solution strengthening and, consequently, lower hardness. Although grain size decreases, its contribution is insufficient to compensate for the reduction in hardness resulting from the decreased phase fraction and matrix softening. Further along the NAB region (Figs. 11 and 12), the microstructure stabilizes, with a predominance of the FCC matrix, a reduced contribution of hard secondary phases, and a more uniform grain morphology, corresponding to the continuous decrease and stabilization of hardness. When designing bimetallic structures, regardless of the production method, it is crucial that the interface between the two different materials possesses sufficient bonding strength to withstand the applied stresses without failure. In such cases, failure occurs on one side of the interface during loading rather than within the interface itself. This implies that the bonding strength of the interface is higher than that of the weaker or softer material.

Regarding the hardness results, cf. Fig. 15, it is reasonable to assume that the present bimetallic is generally made up of a hard steel component and a soft bronze component, as well as an interface between them. The deformation behaviour of the bimetallic samples under tensile loading can be divided into three stages: (i) elastic deformation in both steel and NAB regions, (ii) yielding and plastic deformation in the NAB alloy while steel remains in the elastic regime, and (iii) final fracture occurring within the NAB side. This progression is consistent with the difference in yield strength between the two alloys; the NAB alloy yields and deforms plastically much earlier, while the steel remains largely undeformed until failure. This behavior can be attributed to the significant strength mismatch between the two materials. The 410NiMo martensitic stainless steel exhibits a substantially higher yield strength (≈950 MPa) and elastic modulus (≈200 GPa) compared to the NiAl bronze alloy (YS ≈ 240 MPa, E ≈ 120 GPa). Consequently, under tensile loading, plastic deformation is preferentially initiated and localized in the NAB region, which reaches its yield point at much lower stress levels. As a result, the NAB undergoes significant strain accumulation and eventually fails before the stress intensity at the LME crack tips in the stainless steel can reach the critical threshold required for crack propagation. From the stress-strain response, it is evident that the elastic deformation of the bimetallic samples mirrors that of the NAB alloy more than steel, which is reasonable given that the NAB side accommodates most of the strain. However, the total elongation of the bimetallic sample is significantly lower than that of the monolithic NAB sample, despite the localized deformation. This discrepancy is attributed to the fact that strain is concentrated primarily within the softer bronze region, which spans only half the gauge length. Thus, elongation calculated over the full gauge length underestimates the localized ductility of the NAB region.

It can be noted that the presence of LME cracks at the interface may have important implications for the in-service performance of the bimetallic component. Although these cracks did not lead to interfacial failure under monotonic tensile loading in the present study, they represent localized regions of reduced cohesion that can act as stress concentrators. Under service conditions involving cyclic loading, shear stresses, or multiaxial stress states, such defects may promote premature crack initiation and accelerate crack propagation along grain boundaries in the steel adjacent to the interface. In addition, residual stresses introduced during the WAAM process may further exacerbate crack growth from LME-affected regions. Consequently, although the interface demonstrates sufficient load-bearing capacity under the investigated loading conditions, the presence of LME suggests that the long-term durability and fatigue resistance of the bimetallic structure could be compromised if these defects are not mitigated. Future studies focusing on fatigue behavior, crack growth kinetics, and process optimization to reduce LME susceptibility are therefore necessary to fully assess the component's suitability for demanding service environments.

5. Conclusions

This work provides a detailed assessment of the microstructure, texture, and mechanical behaviour of a WAAM-fabricated NAB/410 NiMo stainless steel bimetallic structure. The results reveal strong links between thermal history, dilution, and alloy chemistry in controlling phase evolution, texture selection, and interfacial integrity. These findings offer valuable guidance for optimising WAAM parameters in the manufacture of high-performance multi-material components. Some of the key results are as follows:

1 The NAB/stainless steel bimetallic part was produced using WAAM–GMAW. No lack of fusion, solidification cracking, or porosity was detected at the interface. The only interfacial defect observed was localized LME cracking. These cracks are attributed to liquid bronze penetration along grain boundaries of stainless steel under thermally induced tensile stresses. Although limited in extent, LME represents the governing interfacial degradation mechanism and must be considered in process optimization to ensure long-term structural reliability.
2 The stainless steel region solidified primarily into martensite with some δ-ferrite, α-ferrite and retained austenite. The structure of the steel was also further refined by grain boundary pinning from fine oxide inclusions. A distinct Fe-rich body-centred cubic (BCC) layer ~10–15 μm thick formed at the NAB/steel boundary. The NAB region consisted of α-phase grains accompanied by multiple K phase precipitates. Precipitate fraction and morphology varied along the build height because of different thermal cycles and varying level of dilution from the steel substrate.
3 EBSD analysis showed weak texture in the stainless steel due to successive solid-state transformations. In contrast, NAB exhibited a textured microstructure with strong <101>//BD fibre texture. The final NAB layer displayed weaker, more random texture, attributed to reduced cooling rate, absence of overlying thermal input, and altered scan directions from the weaving strategy.
4 The bimetallic structure achieved an ultimate tensile strength of ~587 MPa and total elongation of ~12%, with fracture consistently occurring in the NAB region away from the interface. Hardness showed a gradual transition from ~350 HV in the steel to ~170 HV

in NAB. Digital image correlation confirmed that strain localised predominantly in the NAB, while the steel portion remained elastic until failure.

CRediT authorship contribution statement

Mahdi Mahmoudiniya: Writing – original draft, Visualization, Methodology, Investigation, Data curation, Conceptualization. **Briek Luyten:** Methodology, Data curation. **Navid Ghavanini:** Methodology, Data curation. **Patricia Verleysen:** Writing – review & editing, Methodology, Data curation. **Marcel Hermans:** Writing – review & editing, Visualization, Validation, Supervision, Resources, Project administration, Methodology, Investigation, Funding acquisition, Conceptualization. **Leo A.I. Kestens:** Writing – review & editing, Visualization, Validation, Supervision, Resources, Project administration, Methodology, Investigation, Funding acquisition, Data curation, Conceptualization.

Declaration of competing interest

The authors declare that they have no known competing financial interests or personal relationships that could have appeared to influence the work reported in this paper.

Acknowledgement

This work was conducted as part of the project *"Grade2XL – Functionally Graded Materials for Extra Large Structures"*, which received funding from the European Union's Horizon 2020 Research and Innovation Programme under Grant Agreement No. 862017.

Data availability

The data necessary to replicate these results cannot be shared currently as it is part of an ongoing study. However, the authors are open to sharing any particular data on request.

References

[1] S. Pattanayak, S.K. Sahoo, Gas metal arc welding based additive manufacturing—a review, CIRP J. Manuf. Sci. Technol. 33 (2021) 398–442, https://doi.org/10.1016/j.cirpj.2021.04.010.
[2] A. Bandyopadhyay, Y. Zhang, B. Onuike, Additive manufacturing of bimetallic structures, Virtual Phys. Prototyp. 17 (2022) 256–294, https://doi.org/10.1080/17452759.2022.2040738.
[3] N.A. Muhammad, T. Shinde, P. Sharma, Review of interface evolution and joint performance in ultrasonic vibration-assisted friction stir welding of aluminum with dissimilar alloys, Nano-Struct. Nano-Objects 44 (2025) 101541, https://doi.org/10.1016/j.nanoso.2025.101541.
[4] H.J. Meigh, Cast and Wrought Aluminium Bronzes: Properties, Processes and Structure, Paperback ed, 2008. Maney, Leeds.
[5] W. Jin, C. Zhang, S. Jin, Y. Tian, D. Wellmann, W. Liu, Wire arc additive manufacturing of stainless steels: a review, Appl. Sci. 10 (2020) 1563, https://doi.org/10.3390/app10051563.
[6] C. Dharmendra, S. Shakerin, M. Mohammadi, Metallurgical assessment of additive manufactured nickel aluminum Bronze-316L stainless steel bimetallic structure: effect of deposit geometry on the interfacial characteristics and cracking, J. Mater. Eng. Perform. 30 (2021) 8746–8762, https://doi.org/10.1007/s11665-021-06194-1.
[7] Z.H. Liu, D.Q. Zhang, S.L. Sing, C.K. Chua, L.E. Loh, Interfacial characterization of SLM parts in multi-material processing: metallurgical diffusion between 316L stainless steel and C18400 copper alloy, Mater. Char. 94 (2014) 116–125, https://doi.org/10.1016/j.matchar.2014.05.001.
[8] C. Dharmendra, S. Shakerin, G.D.J. Ram, M. Mohammadi, Wire-arc additive manufacturing of nickel aluminum bronze/stainless steel hybrid parts – interfacial characterization, prospects, and problems, Materialia 13 (2020) 100834, https://doi.org/10.1016/j.mtla.2020.100834.
[9] J. Chen, Y. Yang, C. Song, M. Zhang, S. Wu, D. Wang, Interfacial microstructure and mechanical properties of 316L/CuSn10 multi-material bimetallic structure fabricated by selective laser melting, Mater. Sci. Eng., A 752 (2019) 75–85, https://doi.org/10.1016/j.msea.2019.02.097.
[10] X. Zhang, T. Pan, A. Flood, Y. Chen, Y. Zhang, F. Liou, Investigation of copper/stainless steel multi-metallic materials fabricated by laser metal deposition, Mater. Sci. Eng., A 811 (2021) 141071, https://doi.org/10.1016/j.msea.2021.141071.
[11] Y. Li, C. Su, J. Zhu, Comprehensive review of wire arc additive manufacturing: hardware system, physical process, monitoring, property characterization, application and future prospects, Results Eng. 13 (2022) 100330, https://doi.org/10.1016/j.rineng.2021.100330.
[12] D. Svetlizky, M. Das, B. Zheng, A.L. Vyatskikh, S. Bose, A. Bandyopadhyay, J. M. Schoenung, E.J. Lavernia, N. Eliaz, Directed energy deposition (DED) additive manufacturing: physical characteristics, defects, challenges and applications, Mater. Today 49 (2021) 271–295, https://doi.org/10.1016/j.mattod.2021.03.020.
[13] C. Dharmendra, S. Shakerin, M. Mohammadi, Metallurgical assessment of additive manufactured nickel aluminum Bronze-316L stainless steel bimetallic structure: effect of deposit geometry on the interfacial characteristics and cracking, J. Mater. Eng. Perform. (2021), https://doi.org/10.1007/s11665-021-06194-1.
[14] M.H. Razmpoosh, B. Langelier, E. Marzbanrad, H.S. Zurob, N. Zhou, E. Biro, Atomic-scale investigation of liquid-metal-embrittlement crack-path: revealing mechanism and role of grain boundary chemistry, Acta Mater. 204 (2021), https://doi.org/10.1016/j.actamat.2020.116519.
[15] S. Dinda, W.R. Warke, The effect of grain boundary segregation on liquid metal induced embrittlement of steel, Mater. Sci. Eng. 24 (1976) 199–208, https://doi.org/10.1016/0025-5416(76)90113-0.
[16] F. Hasan, A. Jahanafrooz, G.W. Lorimer, N. Ridley, The morphology, crystallography, and chemistry of phases in as-cast nickel-aluminum bronze, Metall. Trans. A 13 (1982) 1337–1345, https://doi.org/10.1007/BF02642870.
[17] B. Li, C. Han, C.W.J. Lim, K. Zhou, Interface formation and deformation behaviors of an additively manufactured nickel-aluminum-bronze/15-5 PH multimaterial via laser-powder directed energy deposition, Mater. Sci. Eng., A 829 (2022) 142101, https://doi.org/10.1016/j.msea.2021.142101.
[18] C. Dharmendra, K. Gururaj, K.G. Pradeep, M. Mohammadi, Characterization of κ-precipitates in wire-arc additive manufactured nickel aluminum bronze: a combined transmission Kikuchi diffraction and atom probe tomography study, Addit. Manuf. 46 (2021) 102137, https://doi.org/10.1016/j.addma.2021.102137.
[19] C. Dharmendra, K.P. Rice, B.S. Amirkhiz, M. Mohammadi, Atom probe tomography study of κ-phases in additively manufactured nickel aluminum bronze in as-built and heat-treated conditions, Mater. Des. 202 (2021) 109541, https://doi.org/10.1016/j.matdes.2021.109541.
[20] C. Dharmendra, K. Gururaj, K.G. Pradeep, M. Mohammadi, Characterization of κ-precipitates in wire-arc additive manufactured nickel aluminum bronze: a combined transmission Kikuchi diffraction and atom probe tomography study, Addit. Manuf. 46 (2021) 102137, https://doi.org/10.1016/j.addma.2021.102137.
[21] X. Yang, D. Liu, S. Kuang, K. Yin, C. Ye, Y. Dong, J. Ju, Z. Shen, S. Ma, L. Fu, A. Shan, Outstanding strength-ductility combination in NAB alloy via coarse Widmanstätten α phases and ultrafine (α+κ) lamella structure, Mater. Sci. Eng., A 920 (2025) 147565, https://doi.org/10.1016/j.msea.2024.147565.
[22] S. Roy, B. Silwal, A. Nycz, M. Noakes, E. Cakmak, P. Nandwana, Y. Yamamoto, Investigating the effect of different shielding gas mixtures on microstructure and mechanical properties of 410 stainless steel fabricated via large scale additive manufacturing, Addit. Manuf. 38 (2021) 101821, https://doi.org/10.1016/j.addma.2020.101821.
[23] S. Roy, B. Shassere, J. Yoder, A. Nycz, M. Noakes, B.K. Narayanan, L. Meyer, J. Paul, N. Sridharan, Mitigating scatter in mechanical properties in AISI 410 fabricated via Arc-based additive manufacturing process, Materials 13 (2020) 4855, https://doi.org/10.3390/ma13214855.
[24] W. Zhai, N. Wu, W. Zhou, Laser metal deposition of low carbon 410L stainless steel and heat treatment, Mater. Sci. Eng., A 872 (2023) 144987, https://doi.org/10.1016/j.msea.2023.144987.
[25] C. Dominique, Transformations in Supermartensitic Stainless Steels, Cambridge University, 2002.
[26] J.C. Lippold, D.J. Kotecki, Welding Metallurgy and Weldability of Stainless Steels, John Wiley, Hoboken, NJ, 2005.
[27] J. Zhang, G. Li, H. Wang, X. Wan, M. Hu, Q. Meng, The effect of non-metallic inclusions in refining microstructure and improving cryogenic toughness of novel high-Mn steel weld metals for LNG tanks, Weld. World 66 (2022) 2281–2295, https://doi.org/10.1007/s40194-022-01365-7.
[28] Q. Wang, J. He, Q. Wang, R. Liu, The role of la–ti–al–o complex inclusions in microstructure refinement and toughness enhancement of the coarse-grained heat-affected zone in high-heat-input welding, Metals 15 (2025) 1105, https://doi.org/10.3390/met15101105.
[29] C. Dharmendra, A. Hadadzadeh, B.S. Amirkhiz, G.D. Janaki Ram, M. Mohammadi, Microstructural evolution and mechanical behavior of nickel aluminum bronze Cu-9Al-4Fe-4Ni-1Mn fabricated through wire-arc additive manufacturing, Addit. Manuf. 30 (2019) 100872, https://doi.org/10.1016/j.addma.2019.100872.
[30] S.M. Orzolek, J.K. Semple, C.R. Fisher, Influence of processing on the microstructure of nickel aluminum bronze (NAB), Addit. Manuf. 56 (2022) 102859, https://doi.org/10.1016/j.addma.2022.102859.
[31] A. Zykova, A. Panfilov, A. Chumaevskii, A. Vorontsov, E. Moskvichev, S. Nikonov, D. Gurianov, N. Savchenko, E. Kolubaev, S. Tarasov, In-situ dispersion hardened aluminum bronze/steel composites prepared using a double wire electron beam additive manufacturing, Progr. Addit. Manuf. 8 (2023) 1067–1082, https://doi.org/10.1007/s40964-022-00378-4.
[32] X. Cai, Z. Wang, L. Dong, M. Yang, J. Zhou, F. Xue, Advanced mechanical properties of nickel-aluminum bronze/steel composite structure prepared by wire-arc additive manufacturing, Mater. Des. 221 (2022) 110969, https://doi.org/10.1016/j.matdes.2022.110969.
[33] C. Shen, G. Mu, X. Hua, F. Li, D. Luo, X. Ji, C. Zhang, Influences of postproduction heat treatments on the material anisotropy of nickel-aluminum bronze fabricated using wire-arc additive manufacturing process, Int. J. Adv. Manuf. Technol. 103 (2019) 3199–3209, https://doi.org/10.1007/s00170-019-03700-7.

[34] Z. Kuai, Z. Li, B. Liu, Y. Chen, H. Li, P. Bai, Microstructure and mechanical properties of CuCrZr/316L hybrid components manufactured using selective laser melting, J. Alloys Compd. 955 (2023) 170103, https://doi.org/10.1016/j.jallcom.2023.170103.
[35] C. Dharmendra, S. Shakerin, G.D.J. Ram, M. Mohammadi, Wire-arc additive manufacturing of nickel aluminum bronze/stainless steel hybrid parts – interfacial characterization, prospects, and problems, Materialia 13 (2020) 100834, https://doi.org/10.1016/j.mtla.2020.100834.
[36] M.H. Razmpoosh, C. DiGiovanni, Y.N. Zhou, E. Biro, Pathway to understand liquid metal embrittlement (LME) in Fe-Zn couple: from fundamentals toward application, Prog. Mater. Sci. 121 (2021) 100798, https://doi.org/10.1016/j.pmatsci.2021.100798.
[37] M. Mahmoudiniya, M.J.M. Hermans, L.A.I. Kestens, Grain boundary susceptibility to liquid metal embrittlement during wire arc additive manufacturing of a bronze/stainless steel bimetallic structure, Mater. Char. 224 (2025) 115058, https://doi.org/10.1016/j.matchar.2025.115058.
[38] O. Andreau, I. Koutiri, P. Peyre, J.D. Penot, N. Saintier, E. Pessard, T. De Terris, C. Dupuy, T. Baudin, Texture control of 316L parts by modulation of the melt pool morphology in selective laser melting, J. Mater. Process. Technol. 264 (2019) 21–31, https://doi.org/10.1016/j.jmatprotec.2018.08.049.
[39] D. Ma, A.D. Stoica, Z. Wang, A.M. Beese, Crystallographic texture in an additively manufactured nickel-base superalloy, Mater. Sci. Eng. 684 (2017) 47–53, https://doi.org/10.1016/j.msea.2016.12.028.
[40] R.R. Dehoff, M.M. Kirka, F.A. List, K.A. Unocic, W.J. Sames, Crystallographic texture engineering through novel melt strategies via electron beam melting: inconel 718, Mater. Sci. Technol. 31 (2015) 939–944, https://doi.org/10.1179/1743284714Y.0000000697.
[41] R.W. Fonda, D.J. Rowenhorst, Crystallographic variability in additive manufacturing, IOP Conf. Ser. Mater. Sci. Eng. 1249 (2022) 012007, https://doi.org/10.1088/1757-899X/1249/1/012007.